SANS (USH1G) regulates pre-mRNA splicing by mediating the intra-nuclear transfer of tri-snRNPs from Cajal bodies to nuclear speckles for spliceosome assembly

Adem Yildirim[1], Sina Mozaffari-Jovin[2,3,4,5], Ann-Kathrin Wallisch[1], Jessica Ries[1], Sebastian Ludwig[2], Henning Urlaub[5], Reinhard Lührmann[2], and Uwe Wolfrum[1,5,6]

[1]Molecular Cell Biology, Institute of Molecular Physiology, Johannes Gutenberg-University of Mainz, Germany

[2]Department of Cellular Biochemistry, Max-Planck-Institute for Biophysical Chemistry, Goettingen, Germany

[3]Medical Genetics Research Center, Mashhad University of Medical Sciences, Mashhad, Iran

[4]Department of Medical Genetics, Faculty of Medicine, Mashhad University of Medical Sciences, Mashhad, Iran

[5]Bioanalytical Mass Spectrometry, Max-Planck-Institute for Biophysical Chemistry, Goettingen, Germany

[5]Senior authors

[6]Corresponding Author and Lead Contact:

Uwe Wolfrum
Tel.: + 49-6131-39-25148;
Fax: + 49-6131-39-23815;
E-mail: wolfrum@uni-mainz.de

Abstract

Splicing is catalyzed by the spliceosome, a compositionally dynamic complex assembled stepwise on pre-mRNA. We reveal the link between splicing machinery components with the intrinsically disordered ciliopathy protein SANS. Pathogenic mutations in *SANS/USH1G* lead to Usher syndrome – the most common cause of deaf-blindness. SANS functions has been associated with cytoplasmic processes so far. Here, we show SANS localization in Cajal bodies and nuclear speckles. There SANS interacts with components of spliceosomal complexes and the large splicing cofactor SON and PRPFs of the tri-snRNP complex. SANS is required for the release of tri-snRNPs from Cajal bodies and their recruitment to nuclear speckles. SANS depletion alters spliceosome assembly kinetics, leading to stalled complex A formation, which can be chased to spliced products by the addition of tri-snRNPs. SANS deficiency and *USH1G* mutations affects splicing of genes related to cell proliferation and USH. We provide the first evidence that splicing deregulation may participate at the pathophysiology of Usher syndrome.

Keywords: Usher Syndrome, ciliopathy, Cajal bodies, nuclear speckles, spliceosome, alternative splicing, intra-nuclear transport

Subject Categories: RNA Biology, Molecular Biology of Disease, Neuroscience

Introduction

Pre-mRNA splicing is a fundamental process in eukaryotic cells that occurs in the nucleus. Splicing results in the removal of introns and the ligation of exons in a nascent precursor messenger RNA (pre-mRNA) to form mature RNA (mRNA) (Papasaikas et al, 2015). Alternative splicing allows the inclusion/exclusion of alternative exons in the mRNA that can give rise to the synthesis of multiple alternative protein isoforms from a single genomic locus. Splicing is catalyzed by the spliceosome, a highly dynamic macromolecular complex composed of five small nuclear ribonucleoproteins (U1, U2, U4/U6, U5 snRNPs) and numerous other polypeptides (Papasaikas et al, 2015; Will & Luhrmann, 2011). During each splicing cycle, the spliceosome assembles *de novo* on the pre-mRNA by stepwise recruitment and assembly of the pre-formed snRNPs and non-snRNP proteins (Wahl et al, 2009). Briefly, U1 and U2 snRNPs recognize the 5´ splice site and the branch point site of the pre-mRNA, respectively, to form the complex A. The U4/U6.U5 tri-snRNP is then recruited to the pre-spliceosome (complex A) to form the pre-catalytic spliceosome (complex B). Complex B undergoes conformational and compositional rearrangements, including the release of U1 and U4 snRNPs, yielding the catalytically active complex B*, which catalyzes the first transesterification reaction. After additional rearrangements, complex C is formed catalyzing the second step of splicing which leads to excision of the intron lariat and ligation of the neighboring exons (Novotny et al, 2015; Will & Luhrmann, 2011).

The biogenesis of snRNPs is an intricate process that occurs in cytoplasmic and nuclear compartments (Fischer et al, 2011). Newly synthesized U snRNAs in the nucleus are exported to the cytoplasm for additional maturation steps, such as the assembly of Sm proteins. Subsequently, they are reimported to the nucleus for maturation in Cajal bodies, where the final assembly of U2, U4/U6 and U4/U6.U5 snRNP complexes occurs (Fischer et al, 2011; Neugebauer, 2017; Roithova et al, 2018; Stanek, 2017). Next, mature snRNP complexes are released from Cajal bodies and are transferred to nuclear speckles, where splicing factors are stored to be supplied to active transcription/pre-mRNA splicing sites closely associated with the nuclear speckles (Galganski et al, 2017; Mao et al, 2011) Both sub-nuclear compartments are membrane-less nuclear organelles formed through liquid-liquid phase separation due to multivalent weak protein interactions which assemble condensates with high local concentration of snRNPs (Spannl et al, 2019). Little is known about the molecular transfer between these organelles per se, especially about the transfer of the mature U4/U6.U5 tri-snRNPs from Cajal bodies to nuclear speckles and their subsequent recruitment to pre-spliceosomes.

Conceivably, changes in alternative splicing patterns are important for cell development and differentiation under normal conditions (Calarco et al, 2007; Daguenet et al, 2015). Aberrant splicing patterns and defects in spliceosomal proteins have been implicated in human diseases (Daguenet et al, 2015; Harbour, 2013; Quesada et al, 2012). Notably, pathologic mutations in several genes coding for pre-mRNA-processing factors (PRPF) cause *Retinitis pigmentosa* (RP) (Tanackovic et al, 2011). Here, we demonstrate that defects in a protein related to the syndromic retinal ciliopathy - the human Usher syndrome (USH) affects splicing patterns of genes associated with cell proliferation and USH.

USH is the most frequent cause of inherited combined deaf-blindness, clinically and genetically complex (Mathur & Yang, 2015; Overlack et al, 2011); so far, 10 USH genes have been assigned to three clinical types (USH1-3). USH1 is the most severe form characterized by profound hearing impairment and vestibular dysfunction, and by RP. Myosin VIIa (USH1B) and scaffold proteins such as harmonin (USH1C), whirlin (USH2D) and SANS (USH1G) organize a common USH protein interactome (Wolfrum, 2011). The association of USH proteins with primary cilia, and defects in ciliogenesis and ciliary maintenance caused by their deficiencies characterize the USH disease as a ciliopathy (Bauss et al, 2014; Bujakowska et al, 2017; Jansen et al, 2016; Liu et al, 1997; May-Simera et al, 2017). Ciliopathies are mainly considered as molecular defects in ciliary modules, such as ciliary transport or signaling (May-Simera et al, 2017); however, more recently, ciliopathy genes were also found to be related to the machineries associated with translation and DNA damage-repair processes (Attanasio, 2015; Chaki et al, 2012; Choi et al, 2013; Gascue et al, 2012). In the present study, we provide the first evidence for a molecular and functional link between a ciliary protein, namely the USH1G protein SANS and the pre-mRNA splicing machinery.

The USH1G protein SANS is a scaffold protein harboring several protein-binding domains able to form homodimers (Fig. 1A) (Adato et al, 2005; Sorusch et al, 2017). Like other USH proteins, SANS is essential for auditory hair-cell development and is part of the signal transduction complex at the tips of stereocilia where it forms high-density protein condensates via liquid-liquid phase separation (Caberlotto et al, 2011; He et al, 2019; Lefevre et al, 2008). In the eye, the role of SANS and the ophthalmic pathogenesis pathway for USH1G are less clear. SANS is expressed in the retinal photoreceptor cells, where it organizes networks of USH proteins which may foster mechanical stabilization of the photosensitive ciliary outer segment (May-Simera et al, 2017; Sahly et al, 2012) and participate in intracellular transport processes (Bauss et al, 2014; Maerker et al, 2008; Overlack et al, 2011; Sorusch et al, 2017). Recently, we reported the role of SANS in endocytosis and primary ciliogenesis (Bauss et al, 2014;

Maerker et al, 2008; Sorusch et al, 2019). Here, we demonstrate the interaction of SANS with key components of the splicing machinery including splicing factor 3B subunit 1 (SF3B1) and SON, a large scaffolding protein known as a splicing cofactor. We show that SANS is needed for a correct release of mature tri-snRNPs from Cajal bodies and for their transfer to nuclear splicing speckles required for the assembly of catalytic spliceosomes. By this mechanism SANS controls splicing of target genes including USH genes. Our results suggest that defective alternative splicing of USH genes may underlay the sensorineural disorders caused by pathogenic variations in the *SANS/USH1G* gene.

Results

SANS interacts with the splicing factor SF3B1, PRPF6, and PRPF31

We identified the splicing factor 3B subunit 1 (SF3B1) as a putative SANS binding partner in yeast two-hybrid (Y2H) screens of a retinal cDNA library with the central domain of the USH1G gene *SANS* (SANS_CENT, aa 126-388) (Fig. 1A). SF3B1 (Fig. 1A), also known as SF3b155 or SAP155, is a component of the U2 snRNP complex of the spliceosome (Cretu et al, 2016; Golas et al, 2003). 1:1 Y2H assays confirmed the interaction of SANS_CENT with the central region of SF3B1 (aa 389-500) (Fig. 1B). Reciprocal co-immunoprecipitations (co-IPs) of recombinant proteins co-expressed in HEK293T cells confirmed the interaction of both proteins and delineated the SF3B1_ULM/p14/HEAT1-8 domain and the SANS_CENT domain as binding sites (Fig. 1C, S1A). Co-IPs in Fig. S1B demonstrated that SANS does not bind to the GFP control.

Notably defects in several components of the spliceosomal U4/U6.U5 tri-snRNP lead to RP, the ocular phenotype in USH patients (Tanackovic et al, 2011). This prompted us to examine whether SANS also interacts with other components of the spliceosome. To this end, we selected the U4/U6-specific protein PRPF31, the U5 protein PRPF6 as well as PRPF3 and PRPF4 which are all components of the U4/U6.U5 tri-snRNP complex and linked to RP. Western blot analysis of co-IPs from HEK293T cells co-expressing FLAG-SANS and GFP-PRPF6 or HA-PRPF31, PRPF3 and PRPF4 revealed that both PRPF6 and PRPF31 also interact with SANS through its CENTn domain (Fig. 1D-F and S1B,B´,C,C`). In contrast, PRPF3 and PRPF4 did not (Fig. 1E).

In silico structural analysis of SANS using the online tools FoldIndex© (Prilusky et al, 2005) and DisEMBL™ (Linding et al, 2003) predicted the SANS CENTn domain (aa 120-250) as an intrinsically disordered region (Fig. S1E). Such regions are characteristics of intrinsically

disordered proteins (IDPs) which can bind to diverse proteins in a context-specific manner (Wright & Dyson, 2015) and their weak multivalent interactions are the basis for phase separation in cells (Garcia Quiroz et al, 2019; Saito et al, 2019).

SANS is a nuclear component that interacts with SF3B1 and PRPFs within the nucleus

Next, we addressed where in the cell SANS interacts with the spliceosomal proteins. Immunofluorescence and immunoelectron microscopy demonstrated the localization of SANS in the chromatin-free nucleoplasma of the nucleus (Fig. 1F). Consistently with the nuclear localization of SANS, *in silico* analysis using NLStradamus (Nguyen Ba et al, 2009) predicted a nuclear localization sequence (NLS) in the C-terminus of human SANS (aa436 – RKKILGAVRRRR – aa447) (Fig. 1A). This was confirmed by NucPred, which rated SANS with a high score (0.76) as a putative NLS-containing protein (Brameier et al, 2007). Immunofluorescence also revealed the co-localization of SANS with SF3B1, PRPF6, and PRPF31 in the nucleoplasm (Fig. 1G). This was affirmed by calculated Pearson coefficients above zero (R = 0.4, 0.6, and 0.2, respectively, for SF3B1, PRPF6, and PRPF31) and by fluorescence intensity plots.

In addition, proximity ligation assays (PLAs) with SANS-SF3B1, SANS-PRPF6 and SANS-PRPF31 pairs revealed PLA signals in the nucleus for all three combinations (Fig. 1H), which were absent in the negative controls (Fig. 1I). This data demonstrated a close spatial proximity of the probed proteins (~30-40 nm) indicating the presence of SANS in complexes with SF3B1, PRPF6 and PRPF31. Taken together, our results strongly support the molecular interaction of SANS with the splicing factors SF3B1, PRPF6 and PRPF31 in the nucleus.

SANS binds to spliceosomal complexes

To test whether SANS interacts with spliceosomal snRNPs complexes we performed co-IPs with nuclear extracts from HEK293T cells expressing FLAG-tagged SANS or PRPF4, a core component of the U4/U6.U5 tri-snRNP (Linder et al, 2014) in absence or in the presence of an *in vitro* synthetized MINX pre-mRNA to induce spliceosome formation. We analyzed the snRNAs isolated from resulting precipitates by Northern blotting applying oligonucleotide probes against U1, U2, U4, U5, and U6 snRNAs (Fig. S2). The blots of PRPF4 IPs revealed strong hybridization signals for U4, U5, and U6 snRNAs indicating a strong pull down of the U4/U6.U5 tri-snRNP by PRPF4 in the absence or in the presence of pre-mRNA. In contrast, SANS failed to pull down any of the U4, U5, and U6 snRNAs in the absence of external pre-mRNA indicating that it is not a stable component of the spliceosomal U4/U6.U5 tri-snRNP complex (Fig. S2). Nevertheless, SANS pulled down more spliceosomal snRNAs in the

presence of the MINX pre-mRNA indicating that it interacts with spliceosomes. This data suggests that SANS is not stably associated with snRNAs, but it interacts with the spliceosomal complexes in cells and *in vitro*, thus it may modulate splicing activity by loosly binding.

SANS is localized in nuclear speckles and its depletion alters the speckles morphology

Since splicing factors are stored and modified in nuclear speckles we tested next whether SANS is present in these nuclear bodies (Galganski et al, 2017). We co-stained SANS and the spliceosomal protein SC35/SRSF2, which commonly serves as a marker for nuclear speckles. Deconvolution microscopy revealed the overlap of the fluorescent signals for SANS and SC35 in the nucleus (Fig. 2A), affirmed by merging the fluorescence intensity plots and by the positive value of Pearson correlation coefficient (R = 0.5) (Fig. 2A-A`). 3D-STED super-resolution microscopy demonstrated that SANS does not directly co-localize with SC35, but closely associates with nuclear speckles (Fig. 2B).

The association of SANS in splicing factor-rich nuclear speckles prompted us to analyze the effect of SANS depletion on nuclear speckles. To this end, we depleted SANS in HEK293T cells using validated SANS siRNAs and immunostained cells for SC35 (Fig. 2C and S3A-D; Table S1). Confocal microscopy revealed significantly increased and diffused SC35 speckles when compared with controls. To exclude off-target effects and cell specificity, we performed the same experiment with an additional siRNA (siSANS#2 recognizing a different region of SANS mRNA) and in HeLa cells as a second cell line. These showed similar diffused speckle formation (Figs. S3D and S4A).

These data demonstrated that SANS is localized in nuclear speckles where large amounts of the spliceosome components are present and post-transcriptional splicing occurs (Cremer & Cremer, 2001; Spector, 2006; Spector & Lamond, 2011) suggesting an association of SANS with the splicing machinery.

SANS is also located at the periphery of Cajal bodies and its depletion increases the number of Cajal bodies

The SANS interaction partners identified, namely PRPF6 and PRPF31 are involved in both the U4/U6.U5 tri-snRNP assembly and its integration into pre-spliceosomes (complex A) to form pre-catalytic spliceosomes (Schneider et al, 2010; Schutze et al, 2016). The assembly and maturation of the tri-snRNP complex occur in separate membrane-less sub-nuclear compartments, called Cajal bodies (Novotny et al, 2015). After maturation, tri-snRNP complexes are released from Cajal bodies and are transferred to the nuclear speckles to join complex A initiating the formation of complex B and the activation of the spliceosome (Liu et

al, 2006; Novotny et al, 2015; Schaffert et al, 2004; Wang et al, 2018). To investigate a possible role of SANS for the assembly of the tri-snRNP complex in Cajal bodies, we checked the presence of SANS in Cajal bodies by double immunofluorescence staining of SANS and Coilin, a reliable marker for Cajal bodies, in HEK293T (Fig. 2D-D`). Image analyses revealed that SANS localization at the periphery of Cajal bodies. 3D-STED super-resolution microscopy corroborated the co-localization of SANS with Coilin and affirmed SANS at the rim of Cajal bodies (Fig. 2E).

Next, we investigated the role of SANS for the integrity and organization of Cajal bodies analysing the effect SANS knockdown on Cajal bodies. Interestingly, siRNA-mediated depletion of SANS led to increased abundance of Cajal bodies both in HEK293T and in HeLa cells (Fig. 2F-F`and S4B-B`). Consistent with this, knockdown of SANS with a second siRNA (siSANS#2) increased the number of Cajal bodies, despite the milder effect, most probably owing to the lower knockdown efficiency of this siRNA (~50%) compared with siSANS (Fig. S3A, E-E` and Table S1).

Affinity proteomics reveals interactions of SANS with SON in the nucleus

To obtain a comprehensive view of splicing factors associated with SANS in the nucleus, we carried out a proteomic screen by affinity capture of SANS-binding proteins from nuclear extracts. We immunoprecipitated SANS-associated complexes from nuclear extracts of HEK293T cells expressing 3xFLAG-SANS and analyzed the protein content of the immunoprecipitation by mass spectrometry (MS) (Fig. 3A). In the MS data identified 730 proteins from the 3xFLAG-SANS nuclear extract with more than five-fold change in peptide numbers when compared with the mock-transfected control (Table S2A). Gene Ontology enrichment analysis for significantly enriched proteins by DAVID 6.8 (Huang da et al, 2009) revealed “mRNA processing” and “RNA splicing” among the enriched biological processes and “nuclear speckles” as one of the most enriched cellular components (Table S2B-C).

Besides known interactors of SANS (e.g. harmonin/USH1C and whirlin/USH2D (Adato et al. 2005; Sorusch et al. 2017)), we found SON – a large Ser/Arg-related splicing factor – as one of the most enriched proteins (Fig. 3B, Table S2A). SON serves as an important scaffold protein for the organization of splicing factors in nuclear speckles and essential for splicing of genes related to cell proliferation (Lu et al, 2013; Sharma et al, 2010). Reciprocal co-IPs from nuclear extract of HEK293T cells expressing FLAG-SANS revealed efficient pull down of SON with FLAG-SANS as well as co-precipitation of SANS with anti-SON (Fig. 3C-D). In agreement with the interaction of SANS-SON, immunocytochemistry and PLAs revealed co-localization and spatial proximity of SANS and SON in nuclear speckles *in situ* (Fig. 3E-F).

Furthermore, Western blotting of co-IPs for other spliceosomal core proteins demonstrated that SF3B1, PRPF8, hSNU114, and PRPF38 were also co-precipitated with SANS (Fig. 3D). These data corroborate the binding of SANS to spliceosomal complexes in nuclear speckles, and are in agreement with our previous results above (Fig. 2C) showing that SANS is essential for the normal morphology of nuclear speckles.

The tri-snRNP complex accumulates in Cajal bodies of SANS-depleted cells

An increase in the number of Cajal bodies observed after siSANS knock downs (Fig. 2F) has previously been related to defects in the assembly or in the release of tri-snRNP complexes from Cajal bodies (Novotny et al, 2015; Stanek, 2017). To investigate the role of SANS in the formation of mature tri-snRNPs in Cajal bodies, we first co-stained the U4/U6-specific protein PRPF31 and Coilin in SANS-depleted cells. Confocal microscopy showed the accumulation of PRPF31 in Cajal bodies of SANS-depleted cells when compared with controls (Fig. 4A). Notably, a similar accumulation of PRPF31 in Cajal bodies was previously observed due to tri-snRNP assembly defects after depletion of the U5 protein PRPF6 (Novotny et al, 2015) that we also reproduced (Fig. S4C). In addition, *RNA-FISH* followed by staining for Coilin revealed that U4, U6, and U5 snRNAs accumulated in Cajal bodies in SANS-depleted cells (Fig. 4C-F). Thus, SANS deficiency leads to significant accumulation of tri-snRNP complexes within Cajal bodies.

Next, we addressed the question of whether SANS deficiency also affects the integrity of tri-snRNPs in the nucleus. We depleted SANS in HEK293T cells stably expressing the FLAG-tagged U4/U6 snRNP protein PRPF4 and pulled down the tri-snRNP complex from nuclear extract by immunoprecipitating FLAG-PRPF4. MS analysis revealed no significant changes neither in the peptide number of components of the tri-snRNP complex nor in its composition when compared with the control (Fig. 5A, Table S3). This was confirmed by glycerol gradient fractionation of nuclear extracts (Fig. S5A). For this, we isolated RNA from the gradient fractions and analyzed their tri-snRNP content by Northern blotting using probes for snRNAs. We did not observe significant defects in tri-snRNP formation between nuclear extracts of SANS-depleted cells and controls; only a slight increase of tri-snRNPs (fraction 17) was detected in SANS-depleted extracts.

Interestingly, the Cajal body scaffold protein Coilin was identified by MS as significantly enriched protein in the tri-snRNP fraction precipitated from the siRNA-mediated SANS-depleted nuclear extract (Table S3, Fig. 5A). We validated this result by immunoprecipitations of tri-snRNP complexes using antibodies against Coilin, PRPF4 and PRPF6 (Fig. 5B). While the levels of PRPF4 and PRPF6 were similar between the tri-snRNPs

precipitated from control and that of the SANS-depleted cells, we observed an increased binding of Coilin to tri-snRNPs precipitated from the SANS-depleted cells (Fig. 5B). In conclusion, our data indicated that SANS is not involved in the assembly of the tri-snRNP complexes.

SANS depletion blocks the transfer and recruitment of tri-snRNPs to nuclear speckles

To investigate the role of SANS in the transfer of tri-snRNPs to nuclear speckles, we first co-stained SC35 with the tri-snRNP protein PRPF31, the U2-specific protein SF3B1 or the splicing cofactor SON in SANS-depleted cells. Notably, the PRPF31 staining in nuclear speckles was significantly decreased in SANS-depleted cells (Fig. 5C); PRPF31 was mainly localized in Cajal bodies (Fig. 4A). In contrast, SF3B1 and SON staining slightly but not significantly increased in nuclear speckles of SANS-depleted cells (Figs. 5C` and S5B-C). To examine the formation of spliceosomal complexes in the speckles, we performed *in situ* PLAs to visualize the interaction of SF3B1, SON and PRPF31 with SC35. Interestingly, we found a significant increase in the number of PLA signals for SF3B1-SC35 and SON-SC35 in nuclear speckles of SANS-depleted cells compared with the controls (Figs. 5D and S5D). In contrast, PRPF31-SC35 PLA signals were significantly decreased from nuclear speckles of SANS-depleted cells (Figs. 5D and S5D) and consistent with our previous immunostaining results, the Cajal body-specific PLA signals for PRPF31-Coilin interaction significantly increased in these cells (Figs. 4B and 5C`-D`).

Taken together, these results demonstrated that SANS is important for the transfer of the mature tri-snRNP complex to nuclear speckles where tri-snRNPs are stored to be recruited to pre-spliceosomes at pre-mRNA splicing sites. In the absence of SANS mature tri-snRNPs are retained in Cajal bodies leading to the drastic reduction of tri-snRNPs in nuclear speckles, which affects the kinetics of spliceosome assembly at the periphery or within nuclear speckles.

SANS depletion stalls spliceosome assembly at complex A resulting in a delay of complex B formation and inhibition of splicing

Since tri-snRNPs are recruited to the complex A to form fully assembled spliceosomes (complex B), failure in the transfer of tri-snRNP complexes to the nuclear speckles should result in the accumulation of the stalled complex A, and thus should have an impact on splicing per se. To test this, we examined the effects of SANS knockdown on the spliceosome assembly pathway *in vitro*. We assayed spliceosome complex formation on radiolabeled MINX pre-mRNAs using nuclear extracts prepared from control and SANS depleted cells (Fig. 6). Splicing reactions were stopped at different time points and spliceosomal complexes were separated by

native agarose gel electrophoresis. Subsequent autoradiography revealed substantial changes in the kinetics of the formation of the spliceosomal complexes A, B and C (Fig. 6A, lanes 1-14). We observed the accumulation of complex A along with the delayed formation of complexes B and C in SANS-depleted nuclear extracts compared with the control depletion (Fig. 6A-A`, lane 9-11). Quantification of the autoradiographs showed that in the control nuclear extract already after 10 min ~40% of the pre-mRNA were present in complex B, and this increased to ~60% after 20 min (Fig. 6A-A`, lanes 2-4). Furthermore, complex C formation appeared after 20 min (Fig. 6A-A`, lanes 3–7). In contrast, in SANS-depleted nuclear extracts, complex A was stalled and the formation of complex B was significantly retarded, reaching only ~40% after 30 min, and could not chase to complex C (Fig. 6A-A`, lanes 9-11).

Next, we tested whether the stalled complex A upon SANS depletion is a functional intermediate or a dead-end complex. For this, the accumulated complex A in SANS-depleted nuclear extract was rescued by supplementing with the wild-type nuclear extract (Fig. 6A-A`, lanes 15-32). Autoradiography analysis revealed an effective rescue of the stalled complex A chased to B, followed by complex C formation (Fig. 6A-A´, lanes 19–23 and 28–32).

Owing to the altered kinetics of spliceosome assembly, we next tested the *in vitro* splicing of pre-mRNA with control and SANS-depleted nuclear extracts. Aliquots were taken at various time points of the MINX pre-mRNA splicing reaction; this was followed by RNA isolation and separation of splicing products by denaturing PAGE (Fig. 6B). Quantification of the autoradiographs from three independent experiments revealed that at 120 min only 37% of the pre-mRNA was spliced in siRNA-mediated SANS-depleted extract, while 56% of the pre-mRNA was already spliced in the control reaction (Fig. 6B`). The impaired splicing was fully rescued by the addition of wild-type nuclear extract to the SANS-depleted extract after 30 min, yielding ~50% of spliced mRNA (Fig. 6B`). Therefore, the reduced kinetics of spliceosome assembly upon SANS depletion gives rise to impaired pre-mRNA splicing *in vitro*.

Purified tri-snRNP complex rescues the complex A in SANS-depleted nuclear extract

Next we tested whether the tri-snRNP complex is the spliceosomal subunit affected in the siRNA-mediated SANS-depleted extract and thus required for rescuing the stalled complex A to the pre-catalytic spliceosome (complex B). To this end, we supplemented SANS-depleted nuclear extracts with purified native tri-snRNPs (Fig. S6). Indeed, the *in vitro* spliceosomal complex formation experiment using radiolabeled MINX pre-mRNA demonstrated that while complex A accumulates in SANS-depleted extract, the addition of the purified tri-snRNPs efficiently rescued complex A to complex B. It is noted that the addition of the purified tri-snRNPs did not change the kinetics of the control reaction. Taken together, our results indicate

that SANS is important for the supply of the tri-snRNP complexes to the sites of active splicing, required for the assembly of the spliceosome complex B.

SANS regulates *in vivo* splicing in liaison with pre-mRNA splicing factors

Next we investigated whether SANS affects *in vivo* splicing of target genes in liaison with core splicing factors. Initially, we analyzed the effects of SANS and PRPF6 depletion on the splicing of *RON (MST1R)* and *USH1C* mini genes expressed in HEK293T cells (Figs. 7A, A`). Analysis of the relative percentage of spliced minigene variants indicated that SANS depletion leads to an accumulation of non-spliced *RON* and *USH1C* pre-mRNAs, respectively by 61% and 29%, as compared with the control siRNA treated cells. In addition, we observed similar results in PRPF6-depleted cells namely 61% and 20%, respectively.

Next, we examined whether SANS also affects the alternative splicing of intrinsic genes in HEK293T cells. For this, we assessed the 19 previously described genes that are alternatively spliced and translated to functional protein isoforms (Fig. 7C, Table S4 and S5) (Papasaikas et al, 2015). We additionally included two USH genes *USH1C* and *MYO7A* (USH1B) that are known to be alternatively spliced (Chen et al, 1996; Reiners et al, 2003). After siRNA knockdowns, we isolated mRNA from cells followed by RT-PCR using splice variant-specific primers to detect alternatively spliced products. As an example, in Figure 7B, we show the analyses of the two genes *CCNE1* and *USH1C*, demonstrating a highly significant change in skipping exon 9 or exon 11, respectively (p values <0.005). The splicing perturbation is shown by using percent-spliced-in (PSI) values (presented in scaled Z-scores), which reveal the directional change and magnitude of each splicing event (Fig. 7C, Table S4 and S5). Our results demonstrated that SANS knockdown resulted in a perturbation profile that correlated well with that of PRPF6, PRPF31 and SF3B1 siRNA-mediated knockdowns (Fig. 7C, upper graph, Fig. S3B). As a negative control, we used the knockdown of the serine/arginine-rich splicing factor 1 (SRSF1), which gave rise to a different perturbation profile when compared with SANS or PRPFs knockdowns (Fig. 7C, lower graph, Fig. S3B). Altogether, our results demonstrated that SANS participates in splicing in the cell and that its absence leads to splicing defects similar to those observed for the essential spliceosome proteins SF3B1, PRPF6, and PRPF31.

Depletion of SANS and its spliceosomal interaction partners decreases cell proliferation

Our data indicated that SANS is important for alternative splicing of genes related to cell proliferation (Table S5C). Moreover, functional annotation of SANS interaction partners highlighted the cell cycle as one of the enriched pathways (Table S2). We quantified cell proliferation by WST-1 colorimetric assay after siRNA-mediated knockdown of SANS,

PRPF31, SON, and SRSF1 (validation of siRNAs, Fig. S3B). While SRSF1 depletion reduced cell proliferation only to ~25%, SANS, PRPF31, and SON deficits significantly decreased cell proliferation to more than 80% when compared with controls (Fig. S7, Table S5). This data further confirms that SANS similar to its spliceosomal interaction partners is important for cell proliferation through regulation of alternative splicing of cell proliferation-related genes.

Pathogenic variants of *SANS/USH1G* affect splicing of the *USH1C* gene

In humans, pathogenic variants of *SANS* lead to USH1G, characterized by combined hearing disorder and RP. Since our previous results showed that SANS deficiency significantly change the alternative splicing of the *USH1C* gene, we examined whether pathogenic variants of *SANS/USH1G* can also affect the splicing of *USH1C*. We expressed wild-type or four different pathogenic variants of *SANS*, harboring frame-shift or missense mutations, in cells depleted of endogenous SANS, and analyzed splicing of *USH1C* (Fig. 7D-E). Our data revealed that the expression of wild-type *SANS* restored *USH1C* splicing defect showing that aberrant splicing caused by SANS depletion can be reversed. In contrast, none of the pathogenic variants of *SANS* was able to restore the splicing defect of *USH1C* in SANS-depleted cells (Fig. 7D-E). This demonstrated that pathogenic variants in *SANS* leading to USH1G disrupt the regulatory function of SANS in splicing of target genes.

Discussion

We identified an unexpected link between the ciliary USH1G protein SANS and the splicing machinery of pre-mRNAs. Splicing is catalyzed by the spliceosome, a highly dynamic macromolecular complex with more than 150-200 proteins contributing to the sequential assembly and regulation of the spliceosome (Papasaikas et al, 2015; Will & Luhrmann, 2011). Although previous studies have indicated the participation of SANS in several cellular functions it has not hitherto been related to the splicing machinery. Here, we show that SANS mediates the intra-nuclear transfer of tri-snRNPs between sub-nuclear membrane-less organelles during spliceosome assembly and thereby controls splicing of pre-mRNA (Fig. 8).

SANS interacts through an intrinsically disordered region with proteins of the pre-mRNA splicing machinery in membrane-less organelles of the nucleus

SANS is a multivalent scaffold protein and participates in membrane adhesion complexes (Maerker et al, 2008; Sorusch et al, 2017), is associated with microtubule-based intracellular transport (Adato et al, 2005; Lefevre et al, 2008; Maerker et al, 2008; Overlack et al, 2011; Papal et al, 2013), regulates endocytosis, and is involved in primary ciliogenesis (Bauss et al,

2014). For these functions, SANS interacts with a variety of proteins including several proteins related to the human USH (Adato et al, 2005; Bauss et al, 2014; Caberlotto et al, 2011; Lefevre et al, 2008; Maerker et al, 2008; Overlack et al, 2011; Papal et al, 2013; Sahly et al, 2012; Sorusch et al, 2017) and other ciliopathies (Sorusch et al, 2014). While, PDZ-domain-containing scaffold proteins bind to the type I PDZ-binding motif and the SAM domain at the C-terminus of SANS (Bauss et al, 2014; Maerker et al, 2008; Sorusch et al, 2017; van Wijk et al, 2009), the majority of interacting proteins bind to SANS via the CENT domain (Adato et al, 2005; Overlack et al, 2011; Sorusch et al, 2017).

In the present study, we demonstrate that core proteins of the pre-mRNA splicing machinery namely SF3B1, PRPF6, and PRPF31 interact with SANS in cells through the N-terminal region of the SANS CENT domain (CENTn). While the binary interaction of SANS-SF3B1 was confirmed by both reciprocal co-IPs and Y2H assays, we cannot rule out that the interaction of SANS with PRPF31 and PRPF6 shown by co-IPs can be indirect via other splicing factors. *In silico* structural analysis predicted SANS_CENTn as an intrinsically disordered region (IDR) (Fig. S1D). IDRs can adopt their three-dimensional structures for binding to diverse target proteins in a cell-context-specific manner. This explains the promiscuous interaction of SANS_CENTn with numerous proteins in diverse cellular processes carried out in different cell compartments. Intrinsically disordered proteins (IDPs) are found mainly in macromolecular assemblies and regulate dynamic processes by often transient interactions with target proteins (De Biasio et al, 2014; Wright & Dyson, 2015). By exploiting these properties, SANS may only transiently or weakly interact with spliceosome molecules, which would explain why it has so far not been found in the proteome of purified spliceosomes.

IDPs are resident proteins of membrane-less organelles such as Cajal bodies and nuclear speckles both of which are the nuclear compartments where SANS is localized and its interaction with the spliceosomal complexes occurs. IDPs are known to drive the formation of both organelles by liquid-liquid phase separation (LPPS) (Alberti & Dormann, 2019; Neugebauer, 2017; Protter et al, 2018). Recently, SANS has been shown to generate protein condensates via LPPS as part of the tip-link complex in stereocilia of inner ear hair cells (He et al, 2019). It is thought that SANS can change the material properties in the tip-link complex. In the absence of SANS, the tip-link complex of hair cells loose its integrity (Caberlotto et al, 2011). This feature of SANS is in line with the significant changes in the nuclear speckle morphology and the diffluence of speckles which we observed upon SANS depletion (Fig. 2C, S3D and S4A). Therefore, we suppose that the multivalent properties of SANS also promote

changes in the material properties of nuclear speckles (Banani et al, 2017; Banani et al, 2016), a feature which remains to be further investigated.

SANS has no prominent role in the maturation of the tri-snRNP complex in Cajal bodies but is needed for the release of assembled tri-snRNP complexes from Cajal bodies

Pre-mRNA splicing is a highly dynamic process, characterized by stepwise assembly and release of the spliceosomal U1, U2, U4, U6, and U5 snRNP complexes (Girard et al, 2012; Will & Luhrmann, 2011). Northern-blot analysis of SANS pull downs from nuclear extract did not show enrichment of snRNAs. We concluded that SANS does not directly act as a core splicing factor in the catalytic processes of the splicing. However, under splicing conditions and in the presence of the MINX pre-mRNA, SANS could pull down spliceosomal complexes suggesting a possible role for SANS in the regulation of spliceosome assembly/activity.

The U4/U6.U5 tri-snRNP complex is a protein-rich particle consisting of more than two dozen polypeptides (Will & Luhrmann, 2011), which assembles and fully matures in Cajal bodies within the nucleus. Failure of tri-snRNP complex maturation, e.g. in the absence PRPF6, leads to the accumulation of incomplete/immature tri-snRNP intermediates in Cajal bodies (for confirmation see Fig. S4C) and formation of new Cajal bodies (Novotny et al, 2015; Stanek, 2017), which is thought to be a mechanism that compensates for this maturation defect (Novotny et al, 2015; Stanek, 2017). Notably, we observed a similar phenotype in SANS depleted cells: the number of Cajal bodies is drastically increased and SANS deficiency leads to the accumulation of the U4/U6-specific protein PRPF31 in Cajal bodies. Furthermore, in SANS-depleted cells, RNA-FISH experiments revealed the accumulation of U4, U6, and U5 snRNAs and thus entire tri-snRNP complexes in Cajal bodies. These results may support a role for SANS in the regulation of the tri-snRNP complex assembly which should be evident from the accumulation of the U4/U6 di-snRNP intermediates (Makarova et al, 2002; Schaffert et al, 2004) or from the composition of the isolated tri-snRNP complex. However, analysis of snRNPs by glycerol gradient fractionation as well as the MS analysis in SANS-depleted nuclear extracts showed no significant deficit in the composition of the tri-snRNP complex when compared with those isolated from a wild-type extract (Fig. 5A, B, S5A, S6D and Table S3). In addition, while tri-snRNPs are co-localized with the Cajal body scaffold protein Coilin and thus are located in the core of Cajal bodies, where their assembly is driven (Novotny et al, 2011), microscopic analysis consistently demonstrated SANS at the periphery of Cajal bodies. Taken together, these findings exclude a key function for SANS in the assembly of the tri-snRNP complex in Cajal bodies. Instead they suggest a role for SANS in the liberation of assembled tri-snRNPs from Cajal bodies.

SANS participates in the transfer and recruitment of tri-snRNPs to nuclear speckles fostering the stable assembly of the pre-catalytic spliceosomes

Our microscopy analysis shows the close association of SANS to the nuclear speckles which serve as the nuclear compartment where snRNP and non-snRNP splicing factors are stored to be supplied to transcription/splicing sites at the periphery or within speckles (Galganski et al, 2017; Spector & Lamond, 2011). Here, we show that the depletion of SANS leads to an increase in size and diffluence of the nuclear speckles, the morphological alterations previously found in splicing-inhibited cells (Girard et al, 2012). This phenotype was thought to be due to the release of incomplete spliceosomal sub-complexes from the speckles (Girard et al, 2012) and also confirms to a role of SANS as a multi-valent intrinsically disordered protein in driving phase separation of nuclear speckles proposed above.

Our *in vitro* and *in situ* interaction studies demonstrate that SANS interacts with several components of the spliceosome indicating that SANS binds to spliceosomes and might be involved in the regulation of spliceosome activity. Strikingly our data also reveal interaction of SANS with SON in nuclear speckles (Fig. 3). SON is a large SR-like splicing factor which serves as a scaffolding protein in nuclear speckles. (Ahn et al, 2011). SON acts as an important coactivator in splicing and facilitates the formation/stabilization of spliceosomes on weak splice sites by recruiting other SR proteins such as SC35/SRSF2. Through this function, SON contributes to efficient splicing of genes related to cell cycle progression (Ahn et al, 2011; Lu et al, 2013). Interestingly, our data shows that SANS also promotes splicing of genes related to cell proliferation and apoptosis, and its depletion inhibits cell proliferation. Moreover, we found several SR proteins including SC35/SRSF2 in the SANS affinity proteomics data (Fig. 3B) suggesting that SANS and SON may cooperate as a complex in these activities.

A crucial step before catalytic activation of the spliceosome is the recruitment of the U4/U6.U5 tri-snRNP to complex A, to form the pre-catalytic spliceosomal complex B (Boesler et al, 2016; Liu et al, 2006). Our *in vitro* biochemical assays using SANS-depleted nuclear extract and a model pre-mRNA showed stalling of splicing at complex A corroborating a role for SANS in the formation of stable pre-catalytic spliceosomes (complex B; Fig. 6). Analysis of the recruitment of SON, SF3B1 and PRPF31 to nuclear speckles by double-immunofluorescence staining and PLAs for interaction with SC35 reveals that SANS is requiered to recruit the U4/U6.U5 tri-snRNP component PRPF31, but not SON and the U2 snRNP component SF3B1, to nuclear speckles (Fig. 4 and S5). Conversely, SANS deficiency leads to slight increases in the staining of SON and SF3B1 in nuclear speckles and to significant

increases of PLA signals for SON/SC35 and SF3B1/SC35 complexes, which reflect the *in vivo* accumulation of spliceosomal complexes in nuclear speckles.

Prior to the transfer of the tri-snRNP to nuclear speckles, the assembled complex has to be released from the Cajal bodies. The mechanisms underlying the intra-nuclear transfer processes of snRNPs between nuclear organelles such as Cajal bodies and speckles are yet unknown. Here, we provide an emerging evidence that SANS plays an important role in the release of mature tri-snRNPs from Cajal bodies, and their recruitment to nuclear speckles where assembled spliceosomal complexes are stored for pre-mRNA splicing. Based on our findings described above, we suggest the following mechanism (Fig. 8): the tri-snRNP complexes are assembled in the core of Cajal bodies, diffuse to the periphery where SANS coordinates the release of tri-snRNPs from the Cajal bodies for vectorial movement to the nuclear speckles. In the absence of SANS, the release of the tri-snRNP complexes is inhibited and tri-snRNPs accumulate in Cajal bodies (Fig. 4). This leads to deprivation of tri-snRNPs in nuclear speckles required for the formation of the pre-catalytic spliceosomal complex B. Consequently, the splicing cycle is stalled at complex A leading to significant alterations in splicing kinetics (Fig. 5 and 6). The stalled complex A in the SANS-depleted nuclear extract is not a dead-end complex. It can be chased to complex B by the addition of wild-type nuclear extract or isolated tri-snRNP complexes. Furthermore, overexpression of wild-type SANS can rescue the effect of SANS knockdown and increases splicing activity (Fig. 7E).

SANS is required for correct constitutive and alternative pre-mRNA splicing

The *in vitro* splicing assays with MINX pre-mRNA and splicing experiments in cells including the minigene reporter splicing assays as well as the analysis of alternative splicing of intrinsic intron-containing genes consistently show that SANS has a significant impact on constitutive and alternative pre-mRNA splicing. Strikingly, SANS depletion strongly inhibited constitutive and alternative splicing of the *RON* minigene and the constitutive splicing of the *USH1C* minigene (Fig 7A-A´). In addition, we observed very similar splicing perturbation profiles after the siRNA knockdown of SANS and that of the core components of the spliceosome, namely SF3B1, PRPF6, and PRPF31 (Fig. 7C). In contrast, depletion of SRFS1, a non-snRNP splicing factor known to be involved in splicing regulation (Papasaikas et al, 2015), gave rise to a different perturbation profile. These findings suggest that SANS interacts not only physically, but also functionally, with core components of the pre-mRNA splicing machinery. Thus, the splicing data obtained in cells are in perfect agreement with the *in vitro* biochemical results, in that both underline the importance of SANS for the delivery of tri-snRNP complexes to nuclear speckles, and thereby for the kinetics of spliceosome assembly.

SANS and PRPFs deficiency lead by a common pathomechanism to *Retinitis pigmentosa*

Pathogenic variants in *USH1G* cause human USH1, a ciliopathy characterized by sensory neuronal degenerations leading to profound hearing loss, vestibule dysfunction and vision loss in the form of *Retinitis pigmentosa* (RP) (May-Simera et al, 2017). So far, the pathomechanisms causing human USH1 have been related to dysfunction in membrane adhesions, mechanical stabilization and intracellular transport during development of inner-ear hair cells and in the maintenance of photoreceptor cells (Bauss et al, 2014; Bujakowska et al, 2017; Jansen et al, 2016; Liu et al, 1997; May-Simera et al, 2017). While in the inner ear the essential roles of SANS in hair cell differentiation and at the signal transduction complex at the tips of stereocilia can well explain the pathophysiology in USH1G (Caberlotto et al, 2011; He et al, 2019; Lefevre et al, 2008), the ophthalmic pathogenesis in the retina is still puzzling (Zou et al, 2017). A link between USH1G protein SANS – or any other USH1 proteins – and the splicing machinery of cells has not been reported yet and may be key for the retinal phenotype in USH1G. Here, we provide emerging evidence that perturbation of splicing of target genes, caused by defects in the intra-nuclear delivery and the integration of the U4/U6.U5 tri-snRNP complex in the spliceosome, can participate at the pathogenesis of the human USH1 phenotype.

Interestingly, mutations in several pre-mRNA-processing factors of the U4/U6.U5 tri-snRNP – such as *PRPF31* (RP11), *PRPF6* (RP60), *PRPF8* (RP13), *PRPF3* (RP18), *SNRNP200* (RP33) and *PRPF4* (RP70) – also result in retina-specific phenotypes (Buskin et al, 2018; Matera & Wang, 2014; Tanackovic et al, 2011; Zhao et al, 2009). Our present study shows that deficiencies in PRPFs and SANS cause nearly identical effects on splicing, as observed both in *in vitro* and in cells. Moreover, there are significant congruencies between the phenotypes caused by defects in SANS and by those in PRPF proteins. Recent studies showed that mono-allelic mutations in the *PRPF31* gene disrupt retina-specific splicing programs and affect ciliogenesis (Buskin et al, 2018; Wheway et al, 2015). Equally, we have previously shown that SANS depletion alters ciliogenesis (Bauss et al, 2014; Sorusch et al, 2017). In this study, we demonstrate that SANS depletion affects the splicing programs of other USH1 genes, particularly that of *USH1C*, which is known to be specifically spliced in the retina (Reiners et al, 2003; Verpy et al, 2000). Notably, reduction in expression levels by both the haploinsufficiency of *PRPF31* in RP-type 11 (~60%/~80 in mRNA, 40%-60% reduction in protein level) (Buskin et al, 2018) and the knockdown of *SANS* (~60%/~80 in mRNA, 40% reduction in protein level; present study) significantly affects the splicing of target genes. Our earlier reports showed that pathogenic variations of *SANS* alter the nuclear distribution of SANS proteins (Sorusch et al, 2017). In addition, USH causing pathogenic variants of *SANS* cannot

rescue the splicing defect of *USH1C* (Fig. 7E). These findings suggest that pathogenic mutations of SANS influence the kinetics of splicing, which may lead to splice defects.

Since splicing is a fundamental process that is occurring in many cell types, mutations in tri-snRNP related genes cause retinal phenotype only (in the case of RP) or defects in the retina and the inner ear (in the case of USH). In addition, murine animal models for *Prpf* genes and *Sans/Ush1g* do not recapitulate the human ocular phenotype (Bujakowska et al, 2017; Graziotto et al, 2011; Graziotto et al, 2008; Williams, 2008; Wolfrum, 2011). Pre-mRNA splicing factor deficiency may dysregulate specific splicing programs that are known to be implemented in the human retina (Farkas et al, 2013; Zambelli et al, 2010). Recently, it was shown that the truncated pathogenic form of *PRPF31* protein is only expressed in the ocular cells derived from RP11 patients, while it was absent in the other patient-specific cells tested, and that in the latter the levels of wild-type protein were nearly equal between normal and patient cells (Buskin et al, 2018). It is thought that the expression of the pathogenic variant protein exacerbates the splicing defects, and thus ocular cells are most strongly affected. It should not be concealed that the PRPF pathogenic variants are leading to autosomal dominant RP and USH1G is a recessive disease. However, recent studies show that there are recessive pathogenic variants of the splicing molecules (*CWC27*, *SNRNP200*) also lead to RP (Bujakowska et al, 2017; Xu et al, 2017). Taken together, the pathomechanisms and pathways leading to RP in patients with *PRPF* or *USH1G* pathogenic variants may converge and thereby provide common targets for future therapeutic strategies.

Conclusion

This study has deciphered the nuclear function of the USH1 protein SANS as a pre-mRNA splicing regulator (Fig. 8). In Cajal bodies SANS acts as a factor required for the correct release and recruitment of the tri-snRNP complex to nuclear speckles and thus SANS contributes in the correct assembly of the pre-catalytic spliceosome on target pre-mRNAs. SANS depletion stalls the splicing process at complex A and reduces the kinetics of spliceosome assembly. Consequently, SANS deficiency alters constitutive and alternative splicing of genes related to cell proliferation and to the human USH. Pathogenic variants of *USH1G/SANS* lead to aberrant splice variants of other USH genes which may underlie the pathophysiology of the retinal degenerations associated with USH1G. In addition, our results further support findings of earlier studies, demonstrating that the RP phenotype in the eye can arise from changes in splicing efficiency.

Materials and methods

Antibodies

As primary antibodies were used: polyclonal antibodies against SANS (RpAb) (Overlack et al, 2008; Sorusch et al, 2017), anti-SANS (MmAb) (sc-514418, Santa Cruz), anti-FLAG (F1804, Sigma Aldrich), anti-PRPF6 (sc-48786, Santa Cruz), anti-HA (Roche), anti-GFP (ab6556, Abcam), anti-PRPF31 (PAB7154, Abnova), anti-hSNU114 (Fabrizio et al, 1997), anti-Coilin (sc-55594, Santa Cruz), anti-SC35 (sc-53518, Santa Cruz), anti-SON (ATLAS, HPA023535), anti-SF3B1 (MmAb) (sc-514655, Santa Cruz), anti-SF3B1 (RmAb)(Will et al 2001), and anti-PRPF38 (homemade). Secondary antibodies were conjugated to the following fluorophores: Alexa488 (donkey-anti-rabbit, A21206, Molecular Probes, Eugene, USA), CF 488 (donkey-anti-guinea pig, 20169-1, Biotrend, Destin, USA), Alexa488 (donkey-anti-mouse, A21202, Molecular Probes), Alexa 555 (donkey-anti-mouse, A31570, Molecular Probes), Alexa 568 (donkey-anti-rabbit, A10043, Invitrogen, Karlsruhe, Germany) CF640 (donkey-anti-goat, 20179-1, Biotrend), Alexa 680 (donkey-anti-goat, A21084, Molecular Probes), Alexa 680 (goat-anti-rat, A21096, Molecular Probes) Alexa 680 (donkey-anti-rabbit, A10043), IRDye 800 (donkey-anti-mouse, 610-732-124, Rockland, Limerick, USA), Abberior STAR Orange (goat-anti-mouse, Abberior, Göttingen, Germany), and Abberior STAR Red (goat-anti-Rabbit, Abberior, Göttingen, Germany). Nuclear DNA was stained with DAPI (4',6-diamidino-2-phenylindole) (1 mg/ml) (Sigma-Aldrich).

DNA constructs

3xFLAG-tagged SANS full length and deletion constructs were designed and cloned in house as previously described (Sorusch et al, 2017). HA-PRPF31 constructs were kind gifts from Dr. Utz Fischer (University of Wuerzburg, Germany). Deletion constructs of PRPF31 (N-term (aa1-165), C-term (aa 166-499)) were produced by PCR from the HA-PRPF31 plasmid and cloned into the pcDNA3.1 N-HA vector (Thermo Fisher). Deletion constructs of PRPF6 (NTD (aa 1-126), HAT1-6 (aa 293-592), HAT7-13 (aa 593-941)) were cloned into AcGFP-C1 vector (Addgene: 64607). *RON (MST1R)* minigene was a kind gift from Dr. Julian Koenig (IMB-Mainz), and *USH1C* minigene was amplified from the genomic DNA of HEK293T cells and cloned into the pcDNA5/FRT vector (Thermo Fisher). The pcDNA5/FRT-PRPF4 plasmid was constructed by cloning the PRPF4 gene fused to an N-terminal FLAG/HA tag into the pcDNA5/FRT plasmid (Thermo Fisher).

Yeast two-Hybrid (Y2H)

Yeast two-hybrid (Y2H) screens were performed applying the (HybriZAP, Stratagene,

La Jolla, USA) as previously described (Maerker et al. 2008). The DNA binding domain (pBD) fused to CENT domain of human SANS (amino acids 126-368) (NCBI:NM_173477) and used as bait in a bovine oligo-dT primed retinal cDNA library. The interactions were analyzed by evaluating the activation of the β galactosidase reporter genes. The interaction between a protein pair was detected by staining the yeast clones in the X ß-gal colorimetric filter lift assay (LacZ reporter gene). For reciprocal 1:1 Y2H assay, bovine SF3B1 (aa389-500) prey fused to the DNA-binding domain (BD) of the GAL4 transcription factor and human SANS_CENT domain fused to the DNA-activation domain (AD) of GAL4 transcription factor were used as bait and as prey, respectively. Subsequently, bait and prey were transformed into yeast strains PJ694a and PJ694A, respectively, which were mated and yeast colonies were selected using HIS1, ADE3, LacZ, and MEL1 reporter genes to identify positive interactions confirmed by a X ß-gal colorimetric filter lift assay.

Immunoprecipitations/pull down assays

GFP-TRAP® (Chromotek) was performed according to the manufacturer protocol. Briefly, GFP tagged proteins co-expressed with an indicated 3xFLAG-tagged protein in HEK293T cells. 16 h post-transfection, cells were lysed with Triton X-100 lysis buffer (50 mM Tris–HCl pH 7.5, 150 mM NaCl, and 0.5% Triton X-100) containing protease inhibitor cocktail (PI mix; Roche). Lysates were incubated with the beads for 2h at 4°C followed by several washing steps with 10 mM Tris-HCl pH 7.5, 150 mM NaCl, 0.5 mM EDTA. Bound proteins were eluted with 2x Laemmli buffer, separated by SDS-PAGE followed by Western blotting. FLAG and HA immunoprecipitations (IP) were carried out by using the ANTI-FLAG® (Sigma) and Anti-HA Affinity Gel (Biotool) beads.

Mass spectrometry analysis

Proteins were separated on 4–12% Bis-Tris-HCl (pH 7.0) NuPAGE polyacrylamide gels (Invitrogen) and stained with G-colloidal Coomassie Brilliant Blue. Entire lanes of the Coomassie-stained gel was cut into 23 slices and processed for mass spectrometry as previously described (Fabrizio et al, 2009). A comparison of the number of peptides identified for each protein in two samples is a reliable indication of the relative amount of proteins when they are analyzed using identical chromatographic and mass-spectrometric conditions and the same mass spectrometer.

Cell culture and cell lines

Dulbecco's modified Eagle's medium (DMEM) and DMEM-F12 containing 10% heat-inactivated fetal calf serum (FCS) (Thermo Fisher Scientific) were used to culture human HEK293T, HeLa cells, and murine IMCD3 cells, respectively. Plasmids were delivered to the

cells by using Plus Reagent and Lipofectamine LTX (Invitrogen) following the manufacturer's protocol.

HEK293T cells stably expressing FLAG/HA-tagged human PRPF4 was generated using the pcDNA5/FRT-PRPF4 plasmid and Flp-In-293 cells according to the manufacturer's protocol (Thermo Fisher). Briefly, Flp-In 293 cells were transfected with a 9:1 ratio of pOG44:pcDNA5/FRT-PRPF4 plasmids using Lipofectamine 2000 (Invitrogen) and 48 h post-transfection, cells were selected in medium containing hygromycin. Stable clones resistant to hygromycin were expanded and tested for stable expression of FLAG-PRPF4 by Western blotting.

Knockdown and quantitative RT-PCR

siRNAs against human SANS (IDT), PRPF6 (Sigma), PRPF31 (IDT), SRSF1 (Sigma) SF3B1 (Sigma) and SON (Dharmacon) were purchased as indicated in Table S3. Non-targeting control siRNA (siCtrl) was purchased from IDT. For knockdowns, HEK293T and HeLa cells were transfected with a final concentration of 20 nM siRNAs using Lipofectamine RNAiMAX (Invitrogen) following the manufacturer's protocol. Knockdowns were validated by quantitative PCR (qPCR) using gene specific primers (Table S6) and normalized to *GAPDH*. SANS siRNA knockdown efficiency was also validated by Western blotting and immunofluorescence analysis in HEK293T and HeLa cells (Fig. S3).

Immunocytochemistry and light microscopy

Cells were fixed with methanol for 10 min at -20°C or with 4% Paraformaldehyde (PFA) for 10 min at room temperature (RT) and washed with PBS. Permeabilization was performed with 0.1% Triton-X100 (Roth) for 5 min at RT, followed by washes with PBS and blocking for 45 min with 0.5% cold-water fish gelatin, 0.1% ovalbumin in PBS. Primary antibodies were incubated overnight at 4°C, followed by washing with PBS and incubation with secondary antibodies for 1 h at RT. After three washes, specimens were mounted with Mowiol 4.88 (Hoechst, Frankfurt, Germany) and imaged using a Leica DM6000B microscope (Leica, Bensheim, Germany). For STED microscopy, we applied secondary antibodies from Abberior and imaged specimens on an Abberior 3D-STED Facility Line microscope (Abberior, Göttingen, Germany).

Image processing and quantifications

Image processing was performed using a Leica DM6000B microscope (Leica), Leica imaging and ImageJ/Fiji software (Schindelin et al, 2012; Schindelin et al, 2015). Deconvolutions were carried out with the Leica program by using 5-7 Z-stacks with one iteration step and BlindDeblur Algorithm settings. Relative accumulations in Cajal bodies and nuclear speckles

were quantified by the Cell Profiler program and the mean and standard deviation values were obtained from three independent experiments. The threshold settings were adjusted as follows: Green Channel: Manual threshold: 0.1, Red Channel: Manual threshold 0.1. The primary object size (Cajal bodies) was set in between 1 and 40 diameters.

Pearson correlation coefficient is calculated by Coloc2 plugin in ImageJ/Fiji program.

Electron microscopy

For immunoelectron microscopy we applied a previously established pre-embedding labeling technique (Sedmak et al, 2009; Sedmak & Wolfrum, 2010). Specimen were analyzed and documented in a Tecnai 12 BioTwin transmission electron microscope (FEI, Eindhoven, The Netherlands) as previously described. Images were processed using Adobe Photoshop CS (Adobe Systems).

Proximity ligation assay (PLA)

For *in situ* proximity ligation assay Duolink PLA probes anti-rabbit^{PLUS}, anti-mouse^{MINUS}, and Detection Reagent Red were purchased from Sigma. PLA was performed on the fixed HEK293T cells as described before (Sorusch et al, 2017). Briefly, PFA fixed cells were incubated with the primary antibodies overnight at 4°C, followed by incubation with oligonucleotide-labelled secondary antibodies (PLA probes) for 4 h at 37°C. After several washing steps hybridizing connector oligonucleotides were added and ligation was performed for 30 min at 37°C, to form a closed circle template. This was followed by rolling circle amplification for 100 min, addition of fluorescent-labelled oligonucleotides and analysis by fluorescence microscopy. For the negative controls, samples probed with only one protein specific antibody and paired with either the rabbit or mouse IgG specific oligonucleotide-labelled antibody.

RNA-fluorescence *in situ* hybridization (RNA-FISH)

For RNA-fluorescence *in situ* hybridization, we used previously described snRNA probes 5'-end-labeled with Alexa-488 fluorescent dye (Invitrogen) in HEK293T cells (Schaffert et al, 2004; Taneja et al, 1992). Cells were mounted in Mowiol 4.88 (Hoechst, Frankfurt, Germany) and analyzed with a Leica DM6000B microscope (Leica, Bensheim, Germany).

Cell proliferation assay

The proliferation levels of the cell were tested WST-1 cell proliferation assay (Roche) kit according to the manufacturer's protocol. In brief, after the seeding $5x10^3$ cells/well in 96 well plates, siRNA-mediated knockdowns were performed as previously described above. 72 h after the knockdown cells were treated with 10 µl cell Proliferation Reagent WST-1 and incubated for 4 h at 37°C and 5% CO_2. The metabolic activity of the cells was detected with Vario Skan

Flash (Thermo Fisher Scientific) at 460 nm wavelength to compare the difference between control and siRNA knockdowns.

Analysis of alternative splicing *in vivo*

Total RNAs were isolated and reverse transcribed using the Superscript III enzyme (Invitrogen) following manufacturer's protocol. For the analysis of alternative splicing events of the minigenes and genes, forward and reverse primers against alternatively spliced exons were used to amplify each splice variant with BioTherm Taq polymerase (GeneCraft) (primer list, Table S6). In brief, 48 h after siRNA transfection, minigenes were delivered to the siRNA-depleted cells using Lipofectamine 2000, and 24 h later, cells were harvested. Levels of splice variants were analyzed by TAPE 2200 capillary electrophoresis (Agilent) using high throughput D1000 ScreenTapes (Agilent). Data values were obtained from the 2200 Tape station controller program. Quantifications of the isoform ratios were carried out as previously described (Papasaikas et al, 2015). Briefly, the median percent spliced in (PSI) indexes were obtained from biological triplicates of siRNA knockdowns. These values summarized as robust Z scores according to the effects of each siRNA treatment with the statistical tests explained in (Papasaikas et al, 2015).

***In vitro* splicing and spliceosome assembly assays**

In vitro splicing assays were carried out as previously described (Makarova et al, 2002). Briefly, radioactive [^{32}P]-labelled MINX pre-mRNA was incubated with 40% (v/v) HEK293T nuclear extract in the splicing buffer containing 20 mM HEPES-KOH pH 7.9, 3 mM MgCl2, 65 mM KCl, 2 mM ATP, and 20 mM creatine phosphate at 30°C for the indicated time points. The isolated RNAs were separated on a denaturing 15% polyacrylamide gel containing 7 M urea and the signals were detected by autoradiography. For the analysis of the spliceosomal complex formation, the splicing reactions (20 µl) were stopped at the indicated time points by the addition of 2 µl heparin (5 mg/ml) and were analyzed by 2% native-agarose gel electrophoresis followed by autoradiography. SANS depleted nuclear extracts are prepared from siSANS treated HEK293T cells.

Purification of the tri-snRNP complex and chase experiment

Purification of the tri-snRNP complex from HeLa nuclear extract was performed as previously described (Agafonov et al, 2016) with minor modifications. Briefly, the nuclear extract in the Roeder C buffer containing 20 mM HEPES pH 7.9, 1.5 mM MgCl2, 450 mM KCl, 0.2 mM EDTA and 25% sucrose, was centrifuged two times ½ h at 20,000 rpm. Next, 3 ml of the cleared supernatant was loaded onto a 20-50% sucrose gradient in 20 mM HEPES pH 7.9, 150 mM KCl, 5 mM MgCl2 and 0.1 mM EDTA in a Surespin rotor and centrifuged at 30,000 rpm for

40 h at 4°C. After gradient fractionation, fractions were analyzed by 4–12% NuPAGE (Invitrogen) and the U4, U5 and U6 snRNAs were detected by SYBR gold (Invitrogen) staining. tri-snRNP containing fractionations were pooled and centrifuged overnight in an S58A rotor at 25,000 rpm at 4 °C. Pelleted tri-snRNPs were dissolved in G250 buffer containing 20 mM HEPES pH 7.9, 250 mM KCl, 5 mM MgCl2, 0.1 mM EDTA. To further purify the tri-snRNPs, the sample was loaded onto a 5-20% Sucrose gradient in G150 buffer in a Surespin rotor and centrifuged overnight at 25,000 rpm at 4°C. After analyzing fractions on a 4–12% NuPAGE, tri-snRNP containing fractions were detected by SYBR gold staining. Purified tri-snRNP complex was directly used in the chase experiment at the zero time point.

Glycerol gradient ultracentrifugation

To analyze the levels of snRNPs by gradient fractionation, 200 µg of the siRNA-mediated SNAS depleted HEK293T nuclear extract or the control nuclear extract were diluted with an equal volume of gradient buffer (G150: 20mM HEPES pH 7.9, 150 Mm NaCl, 1.5mM MgCl2 and 0.5mM DTT) and sedimented on linear 4ml 10-30% (v/v) glycerol gradients in the G150 buffer. The ultracentrifugation was performed in a Sorvall TH-660 rotor for 14 h at 29,000 rpm (114,000 × g) and the gradients were separated into 24 fractions. The levels of snRNPs in each fraction were analyzed by Northern blotting using 5′-end radiolabeled DNA probes against U1, U2, U4, U6 and U5 snRNAs, as previously described (Buskin et al, 2018).

Supplementary data

Supplementary figures

Figure S1. Analysis of SANS domains interacting with splicing factors SF3B1, PRPF6 and PRPF31.

Figure S2. Analysis of the interaction of SANS with spliceosomal snRNPs.

Figure S3. Analysis of SANS knockdown on mRNA and protein levels in HEK293T cells.

Figure S4. The effect of SANS and PRPF6 depletion in nuclear bodies in HEK293T and HeLa cells.

Figure S5. SANS depletion affects the nuclear speckle composition.

Figure S6. The purified tri-snRNP complex chases the stalled complex A to complex B in SANS depleted nuclear extracts.

Figure S7. SANS depletion affects cell proliferation.

Supplementary tables

Table S1. siRNAs and quantifications of knockdowns by qPCR

Table S2. Proteomic analysis of nuclear SANS pull down and Gene Ontology enrichment analysis

Table S3. Proteomic analysis of FLAG-PRPF4 Pull down from nuclear extract of the PRPF4 stable cell line depleted of SANS

Table S4. TAPE results

Table S5. The effect of SANS knockdown on cell proliferation

Table S6. Primers used in the study

Author contributions

A.Y. set up and carried out most of the experiments. S.M.J. and A.Y. set up and carried out the *in vitro* splicing assays and generated stable cell lines. A.K.W. and J.R. helped with several Western-blot and immunofluorescence analyses. H.U. and S.M.J carried out the mass-spectrometric analyses. A.Y., S.M.J., and U.W. designed the studies and A.Y. wrote the manuscript under supervision by S.M.J., R.L. and U.W.

Acknowledgments

We thank to Drs. Utz Fischer, Carlo Rivolta and Julian Koenig for providing several plasmids used in the study; Drs. Cyrill Girard, Dimitry Agofanov and Julian Koenig for valuable discussions; IMB Genomics core facility for the support applying capillary electrophoresis; Mrs. Elisabeth Sehn for her technical expertise with TEM and her valuable help. We also thank to Abberior Company for their valuable support on super-resolution microscopy. This work was supported by GeneRED, IPP Programme Mainz, the FAUN-Stiftung, Nuremberg, and the Foundation Fighting Blindness (FFB; grant no. PPA-0717-0719-RAD).

References

Adato A, Michel V, Kikkawa Y, Reiners J, Alagramam KN, Weil D, Yonekawa H, Wolfrum U, El-Amraoui A, Petit C (2005) Interactions in the network of Usher syndrome type 1 proteins. *Hum Mol Genet* **14:** 347-356

Agafonov DE, Kastner B, Dybkov O, Hofele RV, Liu WT, Urlaub H, Luhrmann R, Stark H (2016) Molecular architecture of the human U4/U6.U5 tri-snRNP. *Science* **351:** 1416-1420

Ahn EY, DeKelver RC, Lo MC, Nguyen TA, Matsuura S, Boyapati A, Pandit S, Fu XD, Zhang DE (2011) SON controls cell-cycle progression by coordinated regulation of RNA splicing. *Mol Cell* **42:** 185-198

Alberti S, Dormann D (2019) Liquid-Liquid Phase Separation in Disease. *Annu Rev Genet* **53:** 171-194

Attanasio M (2015) Ciliopathies and DNA damage: an emerging nexus. *Curr Opin Nephrol Hypertens* **24:** 366-370

Banani SF, Lee HO, Hyman AA, Rosen MK (2017) Biomolecular condensates: organizers of cellular biochemistry. *Nat Rev Mol Cell Biol* **18:** 285-298

Banani SF, Rice AM, Peeples WB, Lin Y, Jain S, Parker R, Rosen MK (2016) Compositional Control of Phase-Separated Cellular Bodies. *Cell* **166:** 651-663

Bauss K, Knapp B, Jores P, Roepman R, Kremer H, Wijk EV, Marker T, Wolfrum U (2014) Phosphorylation of the Usher syndrome 1G protein SANS controls Magi2-mediated endocytosis. *Hum Mol Genet* **23:** 3923-3942

Boesler C, Rigo N, Anokhina MM, Tauchert MJ, Agafonov DE, Kastner B, Urlaub H, Ficner R, Will CL, Luhrmann R (2016) A spliceosome intermediate with loosely associated tri-snRNP accumulates in the absence of Prp28 ATPase activity. *Nat Commun* **7:** 11997

Brameier M, Krings A, MacCallum RM (2007) NucPred--predicting nuclear localization of proteins. *Bioinformatics* **23:** 1159-1160

Bujakowska KM, Liu Q, Pierce EA (2017) Photoreceptor Cilia and Retinal Ciliopathies. *Cold Spring Harb Perspect Biol*

Buskin A, Zhu L, Chichagova V, Basu B, Mozaffari-Jovin S, Dolan D, Droop A, Collin J, Bronstein R, Mehrotra S *et al* (2018) Disrupted alternative splicing for genes implicated in splicing and ciliogenesis causes PRPF31 retinitis pigmentosa. *Nat Commun* **9:** 4234

Caberlotto E, Michel V, Foucher I, Bahloul A, Goodyear RJ, Pepermans E, Michalski N, Perfettini I, Alegria-Prevot O, Chardenoux S *et al* (2011) Usher type 1G protein sans is a critical component of the tip-link complex, a structure controlling actin polymerization in stereocilia. *Proc Natl Acad Sci U S A* **108:** 5825-5830

Calarco JA, Saltzman AL, Ip JY, Blencowe BJ (2007) Technologies for the global discovery and analysis of alternative splicing. *Adv Exp Med Biol* **623:** 64-84

Chaki M, Airik R, Ghosh AK, Giles RH, Chen R, Slaats GG, Wang H, Hurd TW, Zhou W, Cluckey A *et al* (2012) Exome capture reveals ZNF423 and CEP164 mutations, linking renal ciliopathies to DNA damage response signaling. *Cell* **150:** 533-548

Chen ZY, Hasson T, Kelley PM, Schwender BJ, Schwartz MF, Ramakrishnan M, Kimberling WJ, Mooseker MS, Corey DP (1996) Molecular cloning and domain structure of human myosin-VIIa, the gene product defective in Usher syndrome 1B. *Genomics* **36:** 440-448

Choi HJ, Lin JR, Vannier JB, Slaats GG, Kile AC, Paulsen RD, Manning DK, Beier DR, Giles RH, Boulton SJ *et al* (2013) NEK8 links the ATR-regulated replication stress response and S phase CDK activity to renal ciliopathies. *Mol Cell* **51:** 423-439

Cremer T, Cremer C (2001) Chromosome territories, nuclear architecture and gene regulation in mammalian cells. *Nat Rev Genet* **2:** 292-301

Cretu C, Schmitzova J, Ponce-Salvatierra A, Dybkov O, De Laurentiis EI, Sharma K, Will CL, Urlaub H, Luhrmann R, Pena V (2016) Molecular Architecture of SF3b and Structural Consequences of Its Cancer-Related Mutations. *Mol Cell* **64:** 307-319

Daguenet E, Dujardin G, Valcarcel J (2015) The pathogenicity of splicing defects: mechanistic insights into pre-mRNA processing inform novel therapeutic approaches. *EMBO Rep* **16:** 1640-1655

De Biasio A, Ibanez de Opakua A, Cordeiro TN, Villate M, Merino N, Sibille N, Lelli M, Diercks T, Bernado P, Blanco FJ (2014) p15PAF is an intrinsically disordered protein with nonrandom structural preferences at sites of interaction with other proteins. *Biophys J* **106:** 865-874

Fabrizio P, Dannenberg J, Dube P, Kastner B, Stark H, Urlaub H, Luhrmann R (2009) The evolutionarily conserved core design of the catalytic activation step of the yeast spliceosome. *Mol Cell* **36:** 593-608

Fabrizio P, Laggerbauer B, Lauber J, Lane WS, Luhrmann R (1997) An evolutionarily conserved U5 snRNP-specific protein is a GTP-binding factor closely related to the ribosomal translocase EF-2. *EMBO J* **16:** 4092-4106

Farkas MH, Grant GR, White JA, Sousa ME, Consugar MB, Pierce EA (2013) Transcriptome analyses of the human retina identify unprecedented transcript diversity and 3.5 Mb of novel transcribed sequence via significant alternative splicing and novel genes. *BMC Genomics* **14:** 486

Fischer U, Englbrecht C, Chari A (2011) Biogenesis of spliceosomal small nuclear ribonucleoproteins. *Wiley Interdiscip Rev RNA* **2:** 718-731

Galganski L, Urbanek MO, Krzyzosiak WJ (2017) Nuclear speckles: molecular organization, biological function and role in disease. *Nucleic Acids Res* **45:** 10350-10368

Garcia Quiroz F, Li NK, Roberts S, Weber P, Dzuricky M, Weitzhandler I, Yingling YG, Chilkoti A (2019) Intrinsically disordered proteins access a range of hysteretic phase separation behaviors. *Sci Adv* **5:** eaax5177

Gascue C, Tan PL, Cardenas-Rodriguez M, Libisch G, Fernandez-Calero T, Liu YP, Astrada S, Robello C, Naya H, Katsanis N *et al* (2012) Direct role of Bardet-Biedl syndrome proteins in transcriptional regulation. *J Cell Sci* **125:** 362-375

Girard C, Will CL, Peng J, Makarov EM, Kastner B, Lemm I, Urlaub H, Hartmuth K, Luhrmann R (2012) Post-transcriptional spliceosomes are retained in nuclear speckles until splicing completion. *Nat Commun* **3:** 994

Golas MM, Sander B, Will CL, Luhrmann R, Stark H (2003) Molecular architecture of the multiprotein splicing factor SF3b. *Science* **300:** 980-984

Graziotto JJ, Farkas MH, Bujakowska K, Deramaudt BM, Zhang Q, Nandrot EF, Inglehearn CF, Bhattacharya SS, Pierce EA (2011) Three gene-targeted mouse models of RNA splicing factor RP show late-onset RPE and retinal degeneration. *Invest Ophthalmol Vis Sci* **52:** 190-198

Graziotto JJ, Inglehearn CF, Pack MA, Pierce EA (2008) Decreased levels of the RNA splicing factor Prpf3 in mice and zebrafish do not cause photoreceptor degeneration. *Invest Ophthalmol Vis Sci* **49:** 3830-3838

Harbour JW (2013) Genomic, prognostic, and cell-signaling advances in uveal melanoma. *Am Soc Clin Oncol Educ Book***:** 388-391

He Y, Li J, Zhang M (2019) Myosin VII, USH1C, and ANKS4B or USH1G Together Form Condensed Molecular Assembly via Liquid-Liquid Phase Separation. *Cell Rep* **29:** 974-986 e974

Huang da W, Sherman BT, Lempicki RA (2009) Systematic and integrative analysis of large gene lists using DAVID bioinformatics resources. *Nat Protoc* **4:** 44-57

Jansen F, Kalbe B, Scholz P, Mikosz M, Wunderlich KA, Kurtenbach S, Nagel-Wolfrum K, Wolfrum U, Hatt H, Osterloh S (2016) Impact of the Usher syndrome on olfaction. *Hum Mol Genet* **25:** 524-533

Lefevre G, Michel V, Weil D, Lepelletier L, Bizard E, Wolfrum U, Hardelin JP, Petit C (2008) A core cochlear phenotype in USH1 mouse mutants implicates fibrous links of the hair bundle in its cohesion, orientation and differential growth. *Development* **135:** 1427-1437

Linder B, Hirmer A, Gal A, Ruther K, Bolz HJ, Winkler C, Laggerbauer B, Fischer U (2014) Identification of a PRPF4 loss-of-function variant that abrogates U4/U6.U5 tri-snRNP integration and is associated with retinitis pigmentosa. *PLoS One* **9:** e111754

Linding R, Jensen LJ, Diella F, Bork P, Gibson TJ, Russell RB (2003) Protein disorder prediction: implications for structural proteomics. *Structure* **11:** 1453-1459

Liu S, Rauhut R, Vornlocher HP, Luhrmann R (2006) The network of protein-protein interactions within the human U4/U6.U5 tri-snRNP. *RNA* **12:** 1418-1430

Liu X, Vansant G, Udovichenko IP, Wolfrum U, Williams DS (1997) Myosin VIIa, the product of the Usher 1B syndrome gene, is concentrated in the connecting cilia of photoreceptor cells. *Cell Motil Cytoskeleton* **37:** 240-252

Lu X, Goke J, Sachs F, Jacques PE, Liang H, Feng B, Bourque G, Bubulya PA, Ng HH (2013) SON connects the splicing-regulatory network with pluripotency in human embryonic stem cells. *Nat Cell Biol* **15:** 1141-1152

Maerker T, van Wijk E, Overlack N, Kersten FF, McGee J, Goldmann T, Sehn E, Roepman R, Walsh EJ, Kremer H *et al* (2008) A novel Usher protein network at the periciliary reloading point between molecular transport machineries in vertebrate photoreceptor cells. *Hum Mol Genet* **17:** 71-86

Makarova OV, Makarov EM, Liu S, Vornlocher HP, Luhrmann R (2002) Protein 61K, encoded by a gene (PRPF31) linked to autosomal dominant retinitis pigmentosa, is required for U4/U6*U5 tri-snRNP formation and pre-mRNA splicing. *EMBO J* **21:** 1148-1157

Mao YS, Zhang B, Spector DL (2011) Biogenesis and function of nuclear bodies. *Trends Genet* **27:** 295-306

Matera AG, Wang Z (2014) A day in the life of the spliceosome. *Nat Rev Mol Cell Biol* **15:** 108-121

Mathur P, Yang J (2015) Usher syndrome: Hearing loss, retinal degeneration and associated abnormalities. *Biochim Biophys Acta* **1852:** 406-420

May-Simera H, Nagel-Wolfrum K, Wolfrum U (2017) Cilia - The sensory antennae in the eye. *Prog Retin Eye Res* **60:** 144-180

Neugebauer KM (2017) Special focus on the Cajal Body. *RNA Biol* **14:** 669-670

Nguyen Ba AN, Pogoutse A, Provart N, Moses AM (2009) NLStradamus: a simple Hidden Markov Model for nuclear localization signal prediction. *BMC Bioinformatics* **10:** 202

Novotny I, Blazikova M, Stanek D, Herman P, Malinsky J (2011) In vivo kinetics of U4/U6.U5 tri-snRNP formation in Cajal bodies. *Mol Biol Cell* **22:** 513-523

Novotny I, Malinova A, Stejskalova E, Mateju D, Klimesova K, Roithova A, Sveda M, Knejzlik Z, Stanek D (2015) SART3-Dependent Accumulation of Incomplete Spliceosomal snRNPs in Cajal Bodies. *Cell Rep*

Overlack N, Kilic D, Bauss K, Marker T, Kremer H, van Wijk E, Wolfrum U (2011) Direct interaction of the Usher syndrome 1G protein SANS and myomegalin in the retina. *Biochim Biophys Acta* **1813:** 1883-1892

Overlack N, Maerker T, Latz M, Nagel-Wolfrum K, Wolfrum U (2008) SANS (USH1G) expression in developing and mature mammalian retina. *Vision Res* **48:** 400-412

Papal S, Cortese M, Legendre K, Sorusch N, Dragavon J, Sahly I, Shorte S, Wolfrum U, Petit C, El-Amraoui A (2013) The giant spectrin betaV couples the molecular motors to phototransduction and Usher syndrome type I proteins along their trafficking route. *Hum Mol Genet* **22:** 3773-3788

Papasaikas P, Tejedor JR, Vigevani L, Valcarcel J (2015) Functional splicing network reveals extensive regulatory potential of the core spliceosomal machinery. *Mol Cell* **57:** 7-22

Prilusky J, Felder CE, Zeev-Ben-Mordehai T, Rydberg EH, Man O, Beckmann JS, Silman I, Sussman JL (2005) FoldIndex: a simple tool to predict whether a given protein sequence is intrinsically unfolded. *Bioinformatics* **21:** 3435-3438

Protter DSW, Rao BS, Van Treeck B, Lin Y, Mizoue L, Rosen MK, Parker R (2018) Intrinsically Disordered Regions Can Contribute Promiscuous Interactions to RNP Granule Assembly. *Cell Rep* **22:** 1401-1412

Quesada V, Ramsay AJ, Lopez-Otin C (2012) Chronic lymphocytic leukemia with SF3B1 mutation. *N Engl J Med* **366:** 2530

Reiners J, Reidel B, El-Amraoui A, Boeda B, Huber I, Petit C, Wolfrum U (2003) Differential distribution of harmonin isoforms and their possible role in Usher-1 protein complexes in mammalian photoreceptor cells. *Invest Ophthalmol Vis Sci* **44:** 5006-5015

Roithova A, Klimesova K, Panek J, Will CL, Luhrmann R, Stanek D, Girard C (2018) The Sm-core mediates the retention of partially-assembled spliceosomal snRNPs in Cajal bodies until their full maturation. *Nucleic Acids Res* **46:** 3774-3790

Sahly I, Dufour E, Schietroma C, Michel V, Bahloul A, Perfettini I, Pepermans E, Estivalet A, Carette D, Aghaie A *et al* (2012) Localization of Usher 1 proteins to the photoreceptor calyceal processes, which are absent from mice. *J Cell Biol* **199:** 381-399

Saito M, Hess D, Eglinger J, Fritsch AW, Kreysing M, Weinert BT, Choudhary C, Matthias P (2019) Acetylation of intrinsically disordered regions regulates phase separation. *Nat Chem Biol* **15:** 51-61

Schaffert N, Hossbach M, Heintzmann R, Achsel T, Luhrmann R (2004) RNAi knockdown of hPrp31 leads to an accumulation of U4/U6 di-snRNPs in Cajal bodies. *EMBO J* **23:** 3000-3009

Schindelin J, Arganda-Carreras I, Frise E, Kaynig V, Longair M, Pietzsch T, Preibisch S, Rueden C, Saalfeld S, Schmid B *et al* (2012) Fiji: an open-source platform for biological-image analysis. *Nat Methods* **9:** 676-682

Schindelin J, Rueden CT, Hiner MC, Eliceiri KW (2015) The ImageJ ecosystem: An open platform for biomedical image analysis. *Mol Reprod Dev* **82:** 518-529

Schneider M, Hsiao HH, Will CL, Giet R, Urlaub H, Luhrmann R (2010) Human PRP4 kinase is required for stable tri-snRNP association during spliceosomal B complex formation. *Nat Struct Mol Biol* **17:** 216-221

Schutze T, Ulrich AK, Apelt L, Will CL, Bartlick N, Seeger M, Weber G, Luhrmann R, Stelzl U, Wahl MC (2016) Multiple protein-protein interactions converging on the Prp38 protein during activation of the human spliceosome. *RNA* **22:** 265-277

Sedmak T, Sehn E, Wolfrum U (2009) Immunoelectron microscopy of vesicle transport to the primary cilium of photoreceptor cells. *Methods Cell Biol* **94:** 259-272

Sedmak T, Wolfrum U (2010) Intraflagellar transport molecules in ciliary and nonciliary cells of the retina. *J Cell Biol* **189:** 171-186

Sharma A, Takata H, Shibahara K, Bubulya A, Bubulya PA (2010) Son is essential for nuclear speckle organization and cell cycle progression. *Mol Biol Cell* **21:** 650-663

Sorusch N, Bauss K, Plutniok J, Samanta A, Knapp B, Nagel-Wolfrum K, Wolfrum U (2017) Characterization of the ternary Usher syndrome SANS/ush2a/whirlin protein complex. *Hum Mol Genet* **26:** 1157-1172

Sorusch N, Wunderlich K, Bauss K, Nagel-Wolfrum K, Wolfrum U (2014) Usher syndrome protein network functions in the retina and their relation to other retinal ciliopathies. *Adv Exp Med Biol* **801:** 527-533

Sorusch N, Yildirim A, Knapp B, Janson J, Fleck W, Scharf C, Wolfrum U (2019) SANS (USH1G) Molecularly Links the Human Usher Syndrome Protein Network to the Intraflagellar Transport Module by Direct Binding to IFT-B Proteins. *Front Cell Dev Biol* **7:** 216

Spannl S, Tereshchenko M, Mastromarco GJ, Ihn SJ, Lee HO (2019) Biomolecular condensates in neurodegeneration and cancer. *Traffic* **20:** 890-911

Spector DL (2006) SnapShot: Cellular bodies. *Cell* **127:** 1071

Spector DL, Lamond AI (2011) Nuclear speckles. *Cold Spring Harb Perspect Biol* **3**

Stanek D (2017) Cajal bodies and snRNPs - friends with benefits. *RNA Biol* **14:** 671-679

Tanackovic G, Ransijn A, Ayuso C, Harper S, Berson EL, Rivolta C (2011) A missense mutation in PRPF6 causes impairment of pre-mRNA splicing and autosomal-dominant retinitis pigmentosa. *Am J Hum Genet* **88:** 643-649

Taneja KL, Lifshitz LM, Fay FS, Singer RH (1992) Poly(A) RNA codistribution with microfilaments: evaluation by in situ hybridization and quantitative digital imaging microscopy. *J Cell Biol* **119:** 1245-1260

van Wijk E, Kersten FF, Kartono A, Mans DA, Brandwijk K, Letteboer SJ, Peters TA, Marker T, Yan X, Cremers CW *et al* (2009) Usher syndrome and Leber congenital amaurosis are molecularly linked via a novel isoform of the centrosomal ninein-like protein. *Hum Mol Genet* **18:** 51-64

Verpy E, Leibovici M, Zwaenepoel I, Liu XZ, Gal A, Salem N, Mansour A, Blanchard S, Kobayashi I, Keats BJ *et al* (2000) A defect in harmonin, a PDZ domain-containing protein expressed in the inner ear sensory hair cells, underlies Usher syndrome type 1C. *Nat Genet* **26:** 51-55

Wahl MC, Will CL, Luhrmann R (2009) The spliceosome: design principles of a dynamic RNP machine. *Cell* **136:** 701-718

Wang K, Wang L, Wang J, Chen S, Shi M, Cheng H (2018) Intronless mRNAs transit through nuclear speckles to gain export competence. *J Cell Biol* **217:** 3912-3929

Wheway G, Schmidts M, Mans DA, Szymanska K, Nguyen TM, Racher H, Phelps IG, Toedt G, Kennedy J, Wunderlich KA *et al* (2015) An siRNA-based functional genomics screen for the identification of regulators of ciliogenesis and ciliopathy genes. *Nat Cell Biol* **17:** 1074-1087

Will CL, Luhrmann R (2011) Spliceosome structure and function. *Cold Spring Harb Perspect Biol* **3**

Williams DS (2008) Usher syndrome: animal models, retinal function of Usher proteins, and prospects for gene therapy. *Vision Res* **48:** 433-441

Wolfrum U (2011) Protein networks related to the Usher syndrome gain insights in the molecular basis of the disease. In *Usher Syndrome*, Ahuja S (ed), 4, pp 51-73. Nova Science Publishers, Inc.

Wright PE, Dyson HJ (2015) Intrinsically disordered proteins in cellular signalling and regulation. *Nat Rev Mol Cell Biol* **16:** 18-29

Xu M, Xie YA, Abouzeid H, Gordon CT, Fiorentino A, Sun Z, Lehman A, Osman IS, Dharmat R, Riveiro-Alvarez R *et al* (2017) Mutations in the Spliceosome Component CWC27 Cause Retinal Degeneration with or without Additional Developmental Anomalies. *Am J Hum Genet* **100:** 592-604

Zambelli F, Pavesi G, Gissi C, Horner DS, Pesole G (2010) Assessment of orthologous splicing isoforms in human and mouse orthologous genes. *BMC Genomics* **11:** 534

Zhao C, Bellur DL, Lu S, Zhao F, Grassi MA, Bowne SJ, Sullivan LS, Daiger SP, Chen LJ, Pang CP *et al* (2009) Autosomal-dominant retinitis pigmentosa caused by a mutation in SNRNP200, a gene required for unwinding of U4/U6 snRNAs. *Am J Hum Genet* **85:** 617-627

Zou J, Chen Q, Almishaal A, Mathur PD, Zheng T, Tian C, Zheng QY, Yang J (2017) The roles of USH1 proteins and PDZ domain-containing USH proteins in USH2 complex integrity in cochlear hair cells. *Hum Mol Genet* **26:** 624-636

Figures

Figure 1

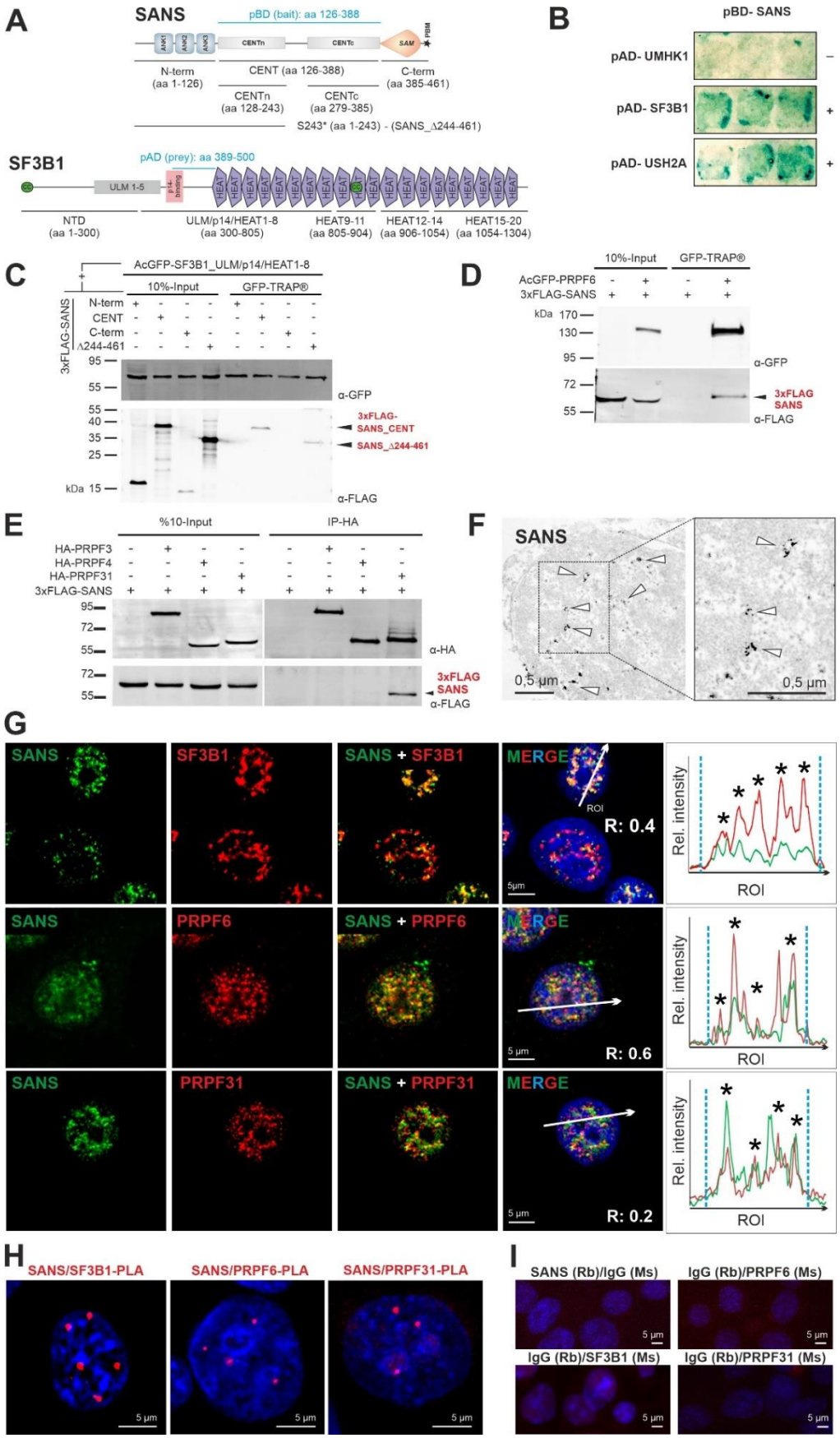

Figure 1. SANS interacts and co-localizes with SF3B1, PRPF6, and PRPF31 in the nucleus. A) Domain structures of SANS and SF3B1. SANS is composed of three ankyrin (ANK) repeats, the central domain (CENT) divided into the N-terminal CENTn and the C-terminal CENTc, the sterile alpha motif (SAM) and C-terminal PDZ binding motif (PBM, *asterisk*). SF3B1 is composed of the N-terminal domain (NTD) including UHM (U2AF-homology motif) ligand motifs (ULM1-5), p14-binding site and 20 HEAT (**H**untingtin, elongation factor 3/**E**F3, protein phosphatase 2A/PP2**A**, and yeast kinase **T**OR1) repeats. At the N-terminal region and in the HEAT10 two coiled-coil domains (CC, green) are present (Cretu et al. 2016). Y2H screen bait and prey (*light blue*) and deletion constructs are indicated. **B)** 1:1 Y2H ß-galactosidase reporter assay shows binding of pBD-SANS_CENT bait to pAD-SF3B1 prey (aa 389-500) containing parts of the p14 and HEAT1 domain (middle panel) and to pAD-USH2A prey (bottom panel), as positive control (Sorush et al. 2019) but not to UMHK1used as negative control. **C)** Western blot analysis of anti-FLAG IPs from cell lysates expressing 3xFLAG-SANS and deletion constructs of acGFP-SF3B1. SF3B1 binds to SANS_CENT and the SANS truncation variant p.S243* (SANS_Δ244-461) revealing CENTn as binding site. **D-E)** Western blot analysis of GFP-TRAP® or anti-HA IPs from HEK293T cells co-expressing 3xFLAG-SANS and GFP-tagged or HA-tagged PRPF31, respectively, demonstrates interaction of SANS with PRPF6 and PRPF31. **F)** Immunoelectron microscopy (anti-SANS RpAb) showing SANS localization (*arrowheads*) in nuclearplasma of a neuron from the inner nuclear layer of a human retina. **G)** Double immunofluorescence of SANS (MmAb) with SF3B1, and SANS (RpAb), PRPF6, and PRPF31 in nuclei of HEK293T cells counterstained with DAPI. Intensity plots for regions of interest in G (*white arrows*) indicate co-localization of SANS with SC35 in nuclear speckles (*asterisks*). Blue vertical dashed lines indicate the nucleus extent. Positive Pearson`s correlation coefficient (R) indicates co-localizations of the two proteins. **H)** PLAs for SANS in combination with SF3B1, PRPF6 or PRPF31 reveal their interaction in the nucleoplasm of HEK293T cells. PFA fixed cells were incubated with specific 1st antibodies followed by incubation with oligonucleotide-labelled 2nd antibodies, anti-rabbitPLUS, anti-mouseMINUS PLA probes, addition of hybridizing connector probes, ligation, rolling circle amplification and imaging by fluorescence microscopy (see methods section). **I)** Negative controls for PLAs in H performed by reciprocal addition of 2nd antibodies.

Figure 2

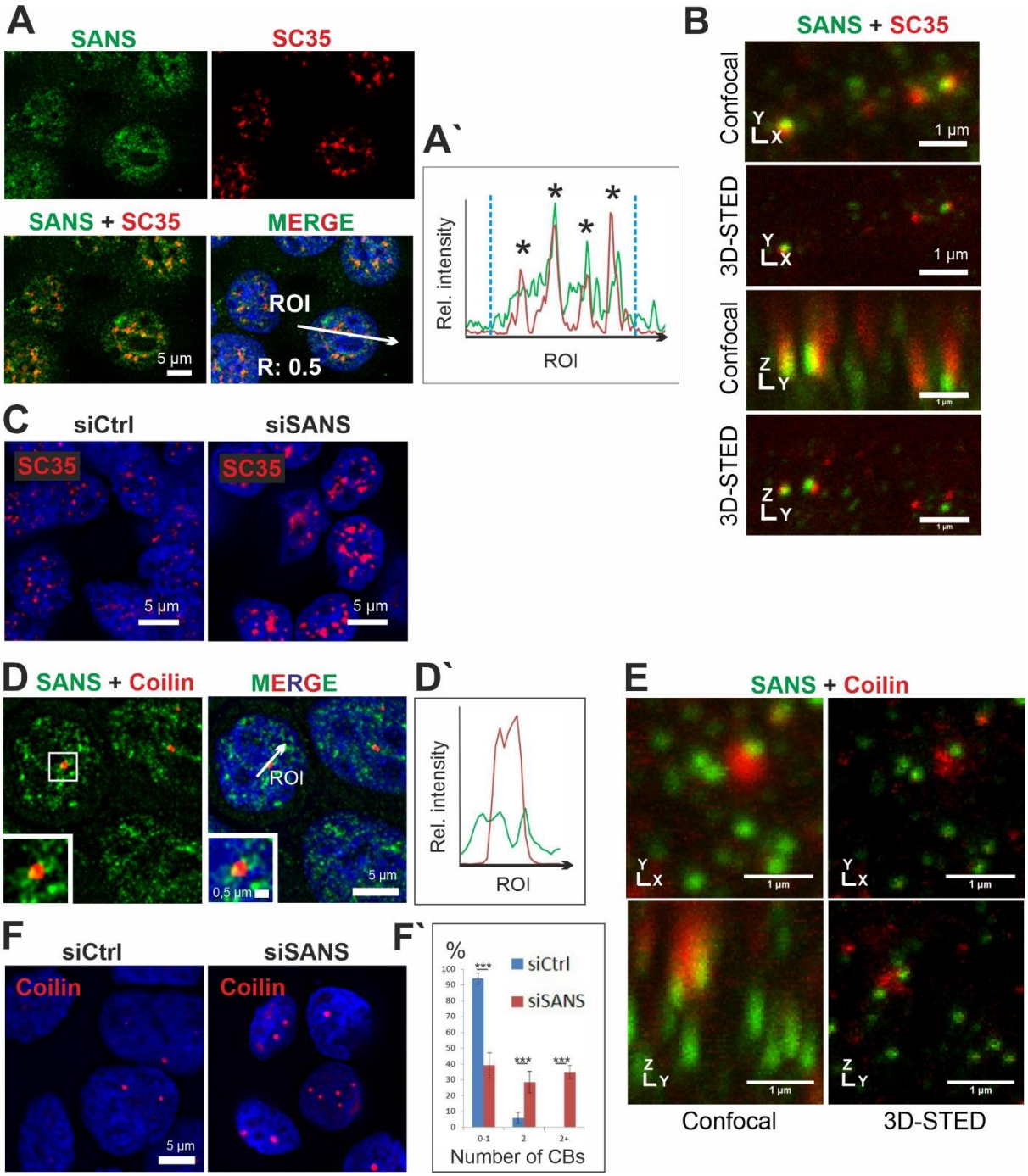

Figure 2. Localization of SANS in nuclear speckles and Cajal bodies. A) Double immunofluorescence staining of SANS (green) and the nuclear speckle marker/spliceosomal protein SC35 (red) in nuclei of HEK293T cells counterstained with DAPI (blue). **A`)** Intensity plots for the regions of interest in A (*white arrows*) indicate co-localization of SANS with SC35 in nuclear speckles (*asterisks*). Blue vertical dashed lines indicate nuclear extensions. Positive Pearson`s correlation coefficient (R) indicates co-localizations of both proteins. **B)** 3D-STED microscopy images of SANS

and SC35 co-stained speckles. XY and YZ axes demonstrate co-localization of SANS with SC35 in nuclear speckles. **C)** Immunofluorescence of SC35 (red) in siRNA-treated HEK293T cells counterstained with DAPI (blue). Nuclear speckles size increases in SANS-depleted cells (siSANS) comparted with control siRNA-treated cells (siCtrl). **D)** Double immunofluorescence of SANS (RpAb, green) and Coilin (red), a molecular marker for Cajal bodies in HEK293T cells counterstained with DAPI (blue). **D`)** Fluorescence intensity plots for region of interest indicated by *arrow* in D reveals SANS localization at the periphery of Cajal bodies in nuclei. **E)** 3D-STED microscopy images of SANS (RpAb, green) and Coilin (red). XY and YZ axes demonstrate localization of SANS at the periphery of Cajal bodies. **F)** Immunofluorescence of Cajal bodies by anti-Coilin (red) in SANS-depleted HEK293T cells. **F`)** Quantification of the number of Cajal bodies (CBs) in SANS-depleted cells; graph shows the percentage of cells with 0-1, 2 or more CBs. SANS depletion increases the number of Cajal bodies in nuclei (200 and 160 cells were counted in siCtrl and siSANS depleted cells, respectively, in 4 independent experiments). ***: p values < 0,001.

Figure 3

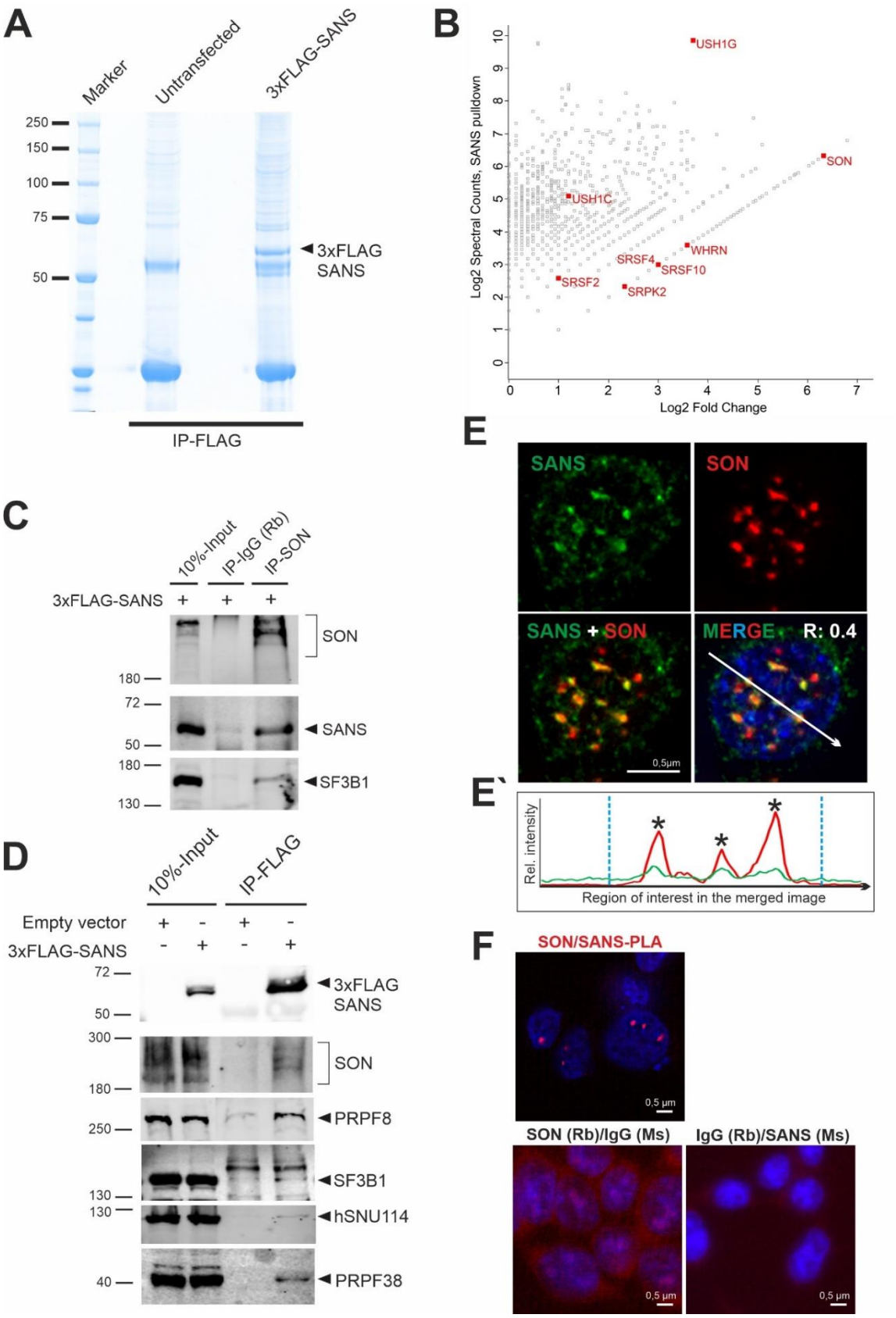

Figure 3. Affinity proteomics and validation of SANS interactions in the nucleus. A) Commassie blue staining of anti-FLAG immunoprecipitated proteins from nuclear extracts of control cells and cells

expressing 3xFLAG-SANS, loaded onto a 4-12% NuPAGE. **B)** Proteomic analysis of SANS interaction partners. Graph displays the relative abundance, in logarithmic scale, of proteins identified in 3xFLAG-SANS pull down from nuclear extract compared with the control. Each dot represent a protein; SR-related splicing factor SON, SR splicing proteins and the SR protein kinase SRPK2 as well as the identified USH proteins are highlighted in red. **C)** Validation of SON-SF3B1-SANS interactions by IP of intrinsic SON in cells expressing 3xFLAG-SANS. SON interacts with SANS and SF3B1. **D)** Western blot analysis of anti-FLAG immunoprecipitations from control and 3xFLAG-SANS nuclear extracts revealed SANS interactions with SON, PRPF8, SF3B1, hSNU114, and PRPF38. **E)** Double immunofluorescence staining of endogenous SANS (MmAb) and SON in HEK293T cells counterstained with DAPI for DNA. Positive Pearson`s correlation coefficient (R) supports co-localization of SANS and SON. **E`)** Fluorescence intensity plots for the region of interest in D (*white arrow*) shows co-localization of SANS with SON in the nucleus. *Blue vertical dashed lines* indicate the extent of the nucleus. **F)** PLAs demonstrate interaction of SANS with SON in cells *in situ*. Red PLA signals are present in the nucleoplasm in SANS-SON PLAs but absent in the negative controls anti-SANS (MmAb) or rabbit anti-SON with mouse and rabbit IgG antibodies.

Figure 4

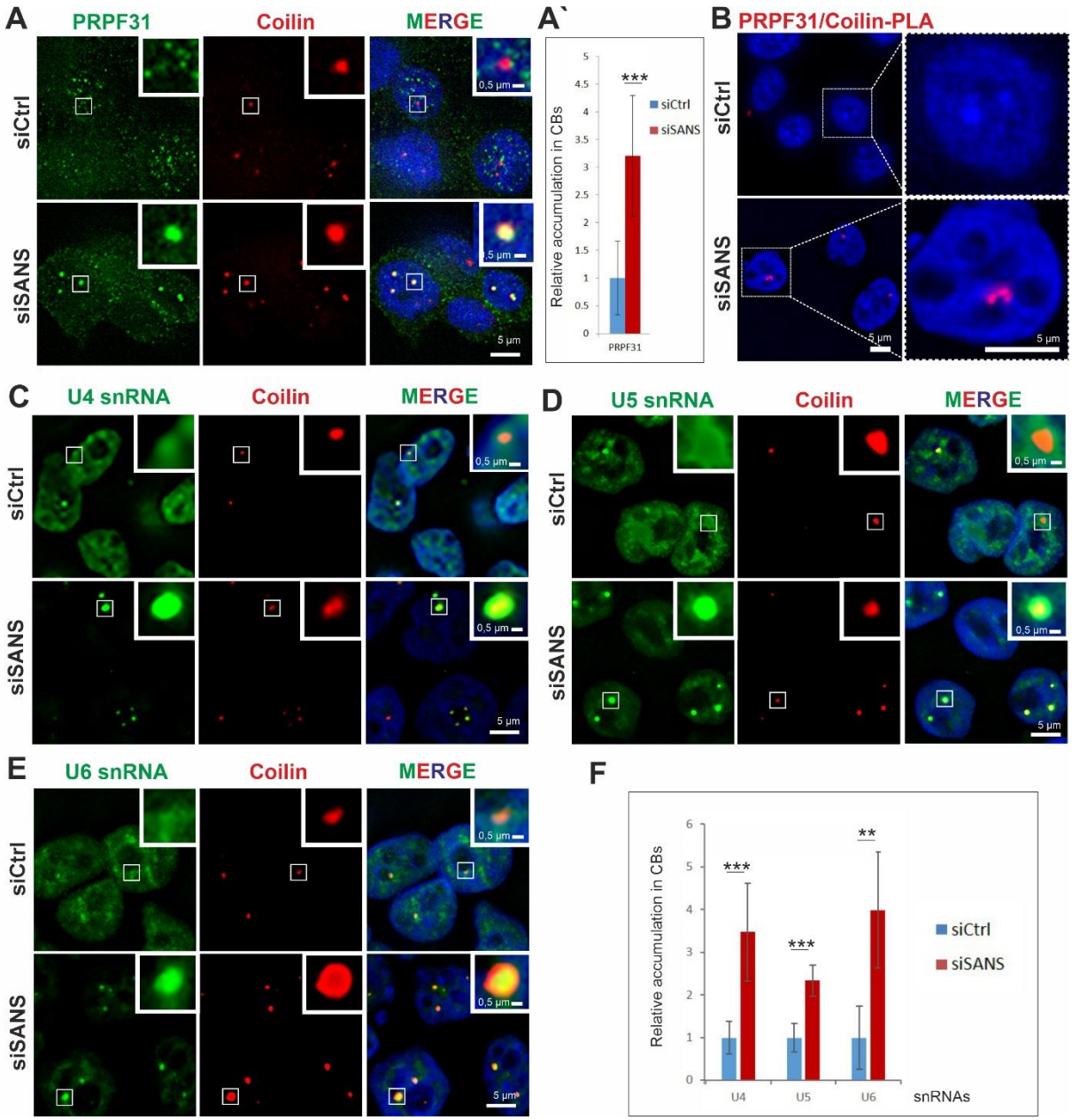

Figure 4. Effects of SANS depletion on Cajal bodies in HEK293T cells. A) Double immunofluorescence staining for Coilin (red) and PRPF31 (green) in siCtrl- and siSANS-treated cells. **A`)** Quantification of PRPF31 signal observed in Cajal bodies reveals accumulation of PRPF31 in Cajal bodies (CBs) in SANS-depleted cells. **B`)** *In situ* PLA assay shows increased PRPF31-Coilin complexes in CBs of SANS-depleted cells. **C-E)** Analysis of *RNA-FISH* labelling of U4, **C**, U5, **D,** and U6, **E,** snRNAs in CBs (Coilin) in siCtrl- and siSANS-treated cells. **F)** Quantification of accumulation of snRNAs in CBs. SANS depletion leads to the significant accumulation of U4, U5 and U6 snRNAs in CBs. Blue, DAPI counterstaining for nuclear DNA. ***: p values < 0.001, **: p values < 0.01.

Figure 5

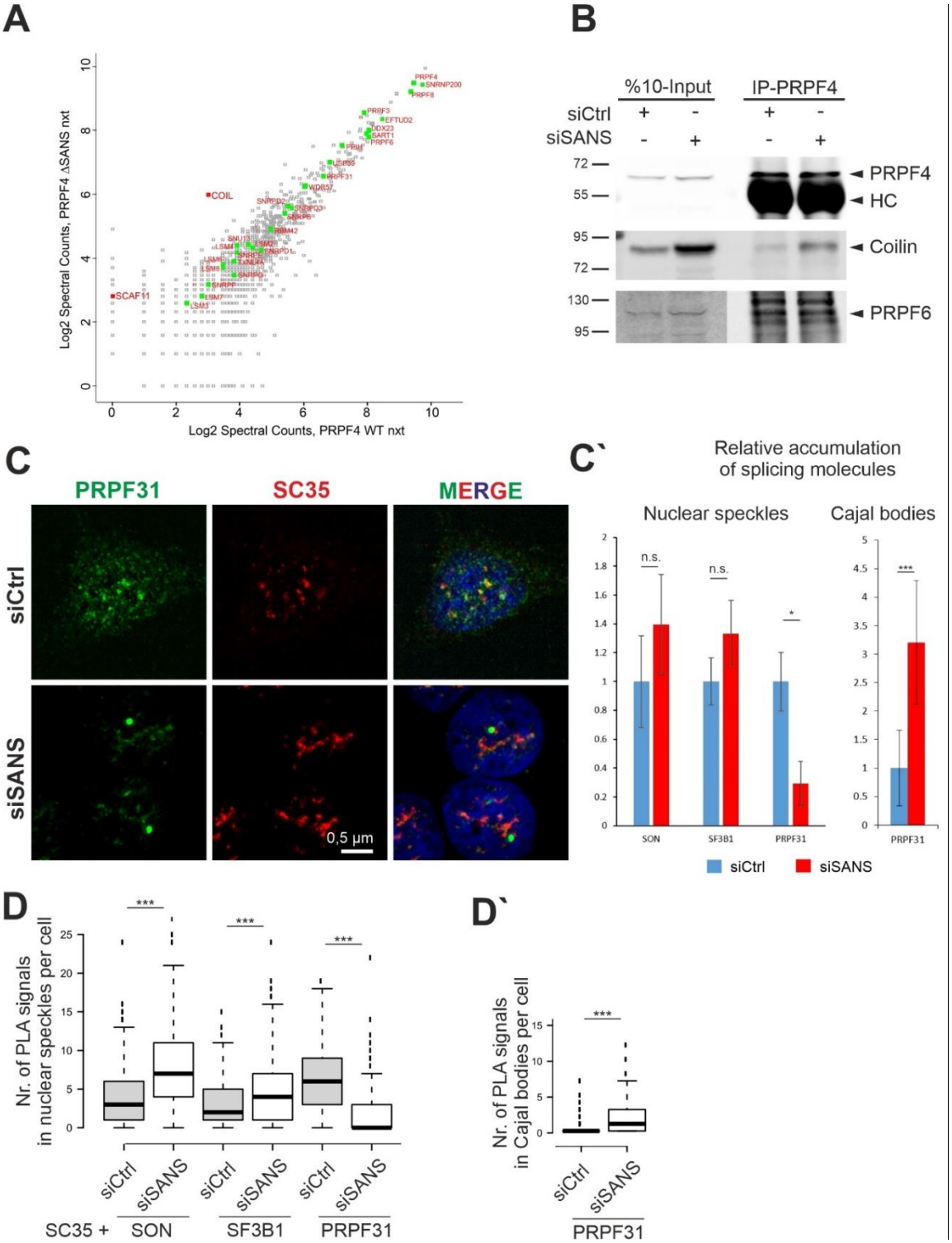

Figure 5: SANS depletion blocks release of tri-snRNP complexes from Cajal bodies and recruitment of mature tri-snRNP complexes to nuclear speckles. A) Proteomic analysis of precipitated tri-snRNP complexes via FLAG-PRPF4 from nuclear extracts of control cells and SANS-depleted cells. Graph displays peptide spectral counts for each protein in logarithmic scale. Green: tri-

snRNPs; red: Coilin (COIL) and SC35-interacting protein (SCAF11). There was no significant change in the composition of the tri-snRNP in SANS-depleted nuclear extract, but the tri-snRNP was largely bound to the Cajal body scaffold protein Coilin. **B)** Western blot analysis of immunoprecipitation of intrinsic PRPF4 from lysates of a HEK293T cell lysates demonstrates stronger interactions of the tri-snRNP protein PRPF4 with Coilin in SANS-depleted cells. SANS depletion does not affect tri-snRNP complex formation visualized by PRPF4 and PRPF6 interaction. **C)** Double immunofluorescence staining reveals reduced PRPF31 staining in SC35 positive nuclear speckles in SANS-depleted cells indicating a defective recruitment of the tri-snRNP complex to nuclear speckles. **C`)** Quantification of immunofluorescence for PRPF31, SON and SF3B1 observed in nuclear speckles and for PRPF31 in Cajal bodies (CB). **D)** Quantifications of PLA signals for SON-, SF3B1- and PRPF31-SC35 show the increase of SON and SF3B1, but a decrease of PRPF31 in nuclear speckles of SANS-depleted cells. **D`)** Quantification of PLA signals for PRPF31-Coilin reveals the accumulation of PRPF31 in Cajal bodies of SANS-depleted cells. P values:***: < 0.001, *: < 0.05.

Figure 6

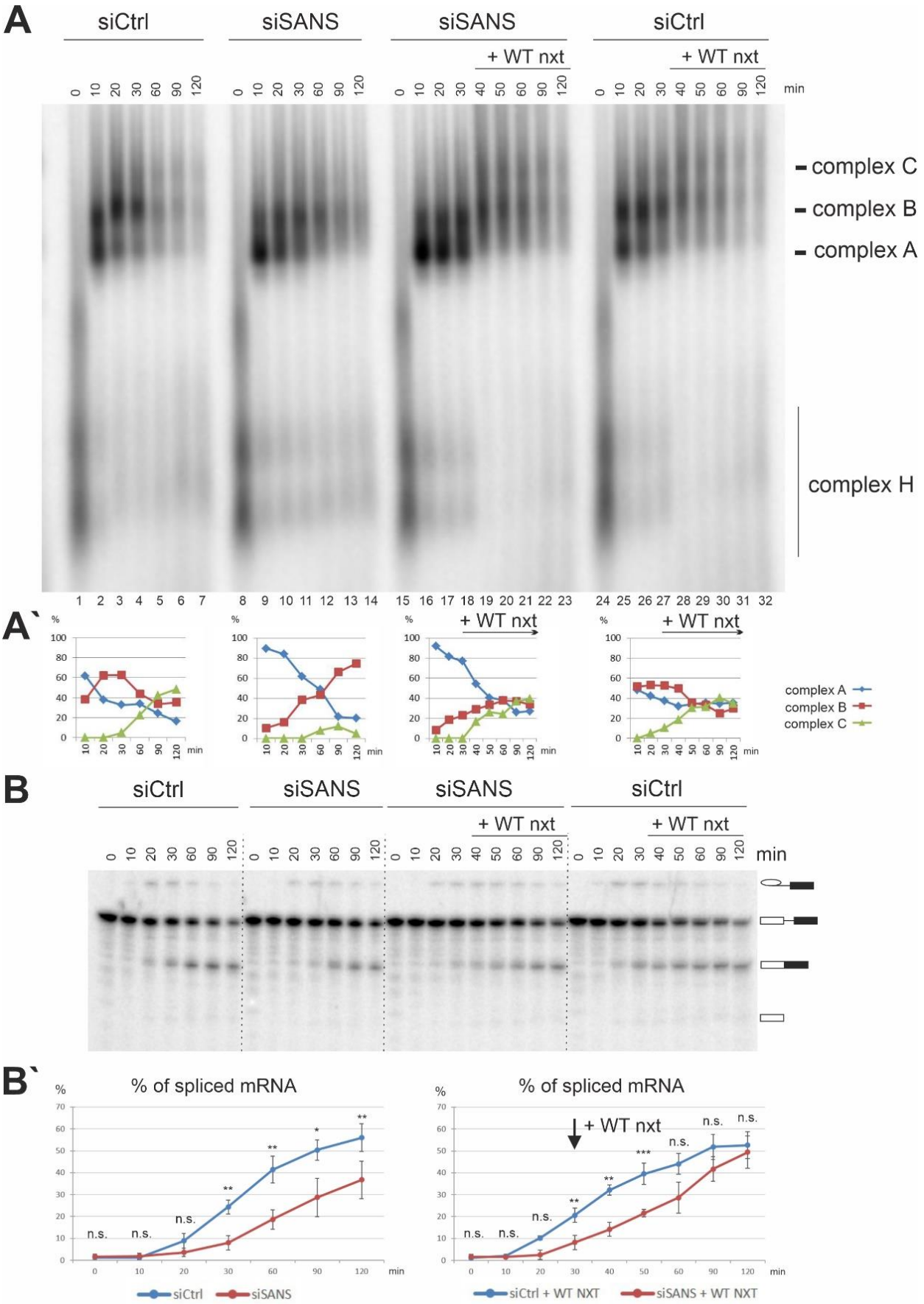
A
siCtrl
siSANS
siSANS
siCtrl
+ WT nxt
+ WT nxt
min
complex C
complex B
complex A
complex H
A`
+ WT nxt
+ WT nxt
complex A
complex B
complex C
B
siCtrl
siSANS
siSANS
siCtrl
+ WT nxt
+ WT nxt
min
B`
% of spliced mRNA
% of spliced mRNA
+ WT nxt
siCtrl
siSANS
siCtrl + WT NXT
siSANS + WT NXT

Figure 6. Analysis of the effects of SANS depletion on spliceosome complex formation and splicing. A) Autoradiography of the time course of assembly of spliceosome complexes on ^{32}P-radiolabelled MINX pre-mRNA analysed by native agarose gel electrophoresis. Splicing reactions were incubated at 30°C for the indicated time points (0-120 min) and stopped by the addition of heparin. The wild type nuclear extract (WT nxt) was added after 30 min to chase the reactions (Lanes: 19-23, 28-32). Positions of each spliceosomal complex are indicated namely complex H, A, B and C. **A`)** lower panel: graphical representation of quantification of complex A, B and C. Depletion of SANS leads to the accumulation of complex A and reduces the level of later complexes. **B)** *In vitro* splicing of ^{32}P radio-labelled MINX pre-mRNA with the control and SANS-depleted nuclear extracts. Splicing of pre-mRNA was analysed by denaturing PAGE followed by autoradiography. **B`)** Quantification of spliced mRNA. Each data point shows an average percentage of spliced mRNA (three independent experiments) for each time point. SANS depletion affects the kinetics of splicing leading to a decreased splicing efficiency (left panel). Addition of WT nxt restores the splicing efficiency (right panel).

Figure 7

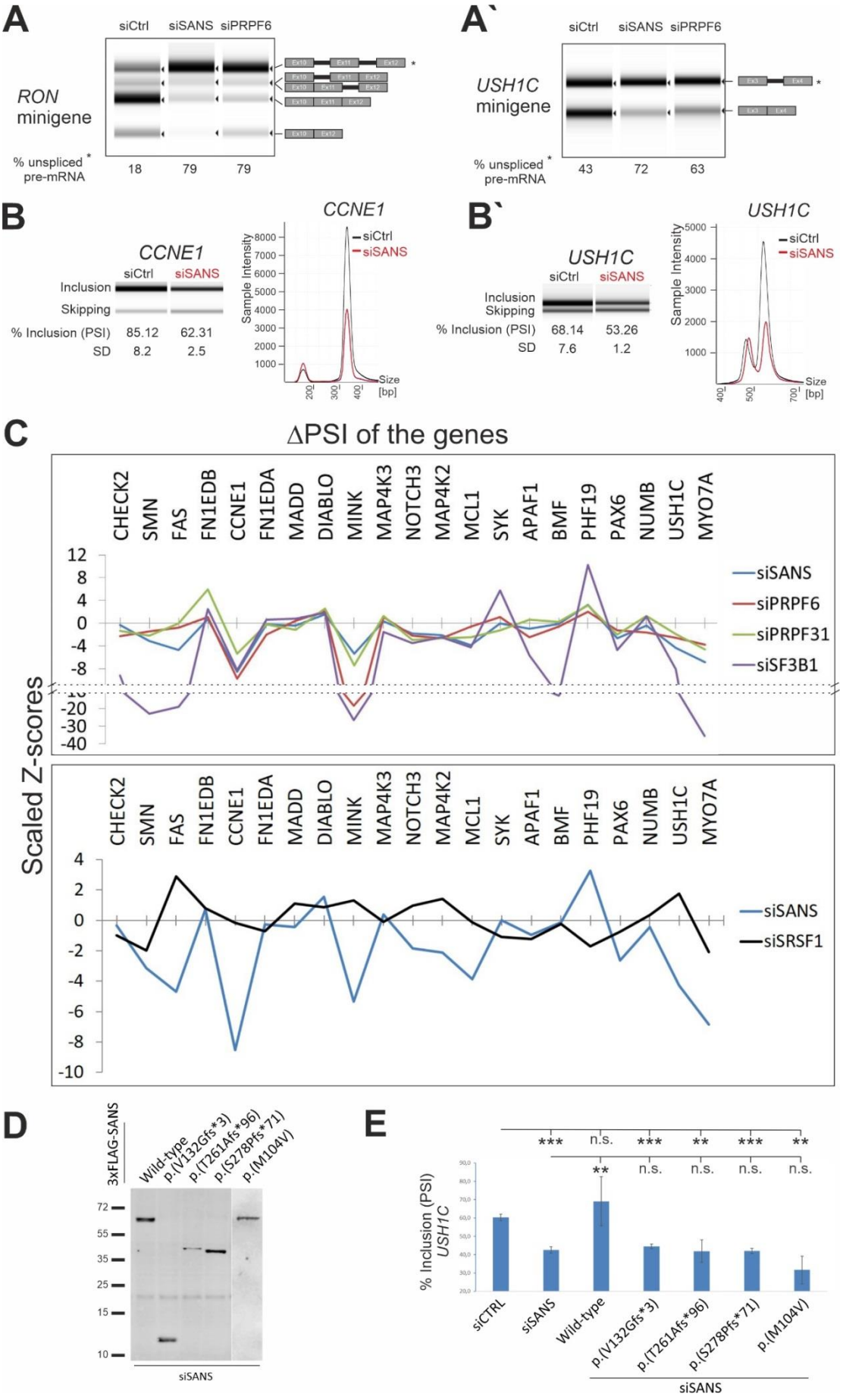
A
siCtrl siSANS siPRPF6
RON minigene
% unspliced * pre-mRNA
18 79 79
A`
siCtrl siSANS siPRPF6
USH1C minigene
% unspliced * pre-mRNA
43 72 63
B
CCNE1
siCtrl siSANS
Inclusion
Skipping
% Inclusion (PSI) 85.12 62.31
SD 8.2 2.5
CCNE1
siCtrl
siSANS
Sample Intensity
Size [bp]
B`
USH1C
siCtrl siSANS
Inclusion
Skipping
% Inclusion (PSI) 68.14 53.26
SD 7.6 1.2
USH1C
siCtrl
siSANS
Sample Intensity
Size [bp]
C
ΔPSI of the genes
CHECK2 SMN FAS FN1EDB CCNE1 FN1EDA MADD DIABLO MINK MAP4K3 NOTCH3 MAP4K2 MCL1 SYK APAF1 BMF PHF19 PAX6 NUMB USH1C MYO7A
siSANS
siPRPF6
siPRPF31
siSF3B1
Scaled Z-scores
siSANS
siSRSF1
D
3xFLAG-SANS
Wild-type
p.(V132Gfs*3)
p.(T261Afs*96)
p.(S278Pfs*71)
p.(M104V)
siSANS
E
% Inclusion (PSI) USH1C
siCTRL
siSANS
Wild-type
p.(V132Gfs*3)
p.(T261Afs*96)
p.(S278Pfs*71)
p.(M104V)
siSANS

Figure 7. SANS regulates *in vivo* splicing of minigene reporters as well as spilcing of genes related to cell proliferation and the human Usher syndrome. A-A´) Splicing of *RON* and *USH1C* minigenes in control, SANS- and PRPF6-depleted cells. Percentage of unspliced mRNA is indicated below the lanes. **B-B´)** High throughput capillary electrophoresis analyses of alternatively spliced variants of the *CCNE1* gene (Exon 9) and *USH1C* (Exon 11) gene after siRNA-mediated depletion of SANS. Relative intensities of the exon included and skipped isoforms obtained from the representative gel images are shown. PSI (% inclusion) and SD indicate, respectively, the percentage spliced-in median and the standard deviation values from three independent experiments. **C)** Graphs showing representative splicing perturbation profiles of selected endogenous genes upon knockdown of *PRPF6*, *PRPF31*, *SF3B1* (upper panel), *SRSF1* (lower panel) or *SANS*, representative for three independent experiments. It is of note that the lines connecting the values measured do not indicate a linkage between the two neighboring genes. Scaled Z-scores represent changes toward inclusion (>0) or skipping (<0) for each alternative splicing event after siRNA-mediated knockdowns. SANS depletion exhibits very similar perturbation profiles as in *PRPF6, PRPF31, and SF3B1* knockdowns (upper panel), but different perturbation profile when compared to that of *SRSF1* (lower panel). Note **D)** Western blot analysis showing the expression of SANS pathogenic variants in the SANS-depleted cells. **E)** Capillary electrophoresis analyses of alternatively spliced variants of *USH1C* (Exon 11) gene after siRNA-mediated depletion of SANS following by overexpression of the wild-type and pathogenic USH1G variants. Only wild-type SANS, but none of the pathogenic *USH1G* variants restored the siSANS-induced splicing deficiency in *USH1C*. Relative intensities of the exon included and skipped isoforms obtained from the representative gel images are shown. Quantification of PSI (% inclusion) and SD values shows the percentage spliced-in median and the standard deviation values from three independent experiments.

Figure 8

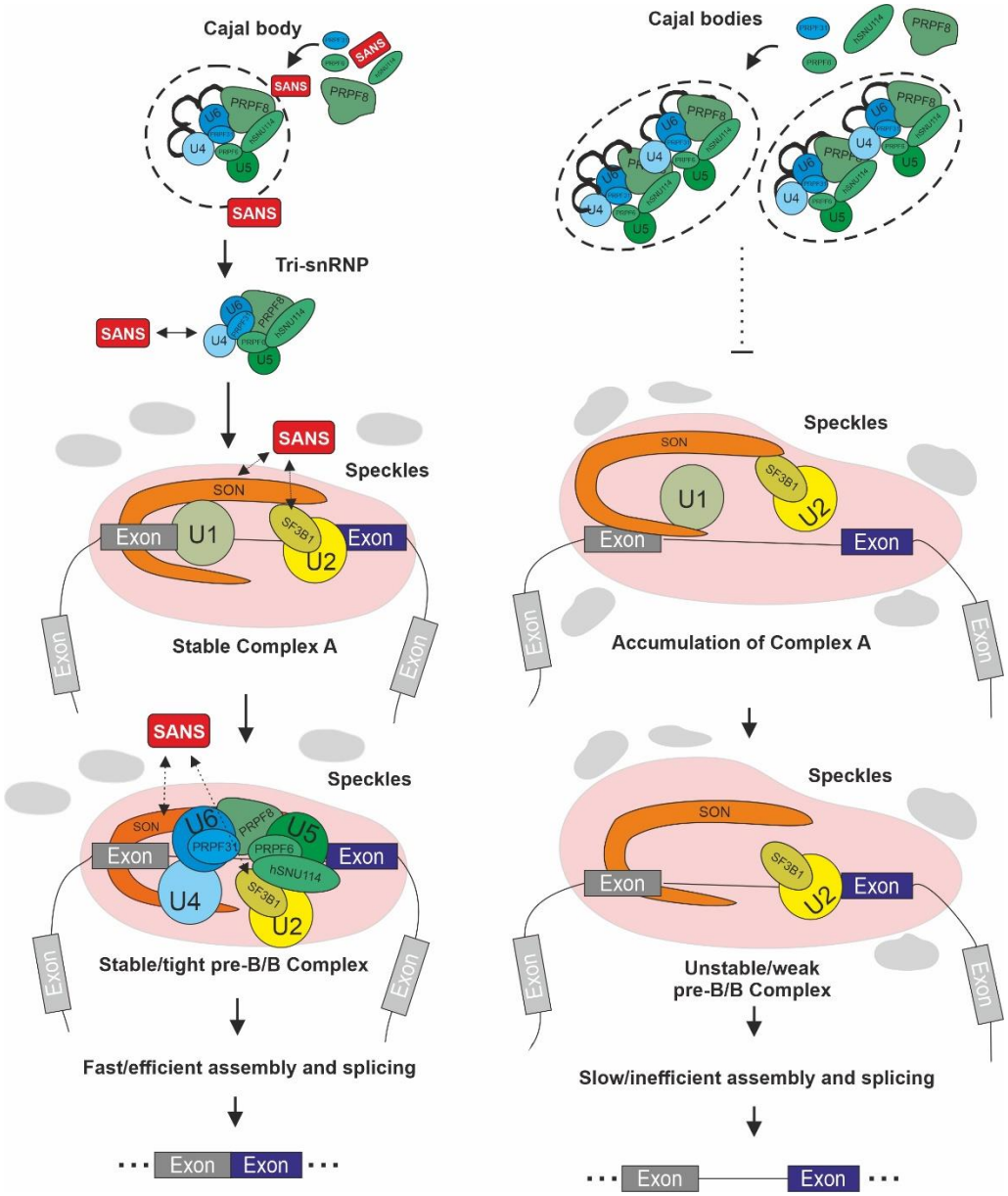

Figure 8. Graphical representation of the role of SANS in the splicing process. In SANS-deficient cells, assembled tri-snRNPs are not released from Cajal bodies and not recruited to nuclear splicing speckles. This leads to the accumulation of tri-snRNP complexes in newly formed Cajal bodies. Furthermore, the reduced level of mature tri-snRNPs in nuclear speckles retards formation of spliceosome Complex B, affecting the kinetics and efficiency of pre-mRNA splicing of target genes.

Supplementary data

Supplementary Figures

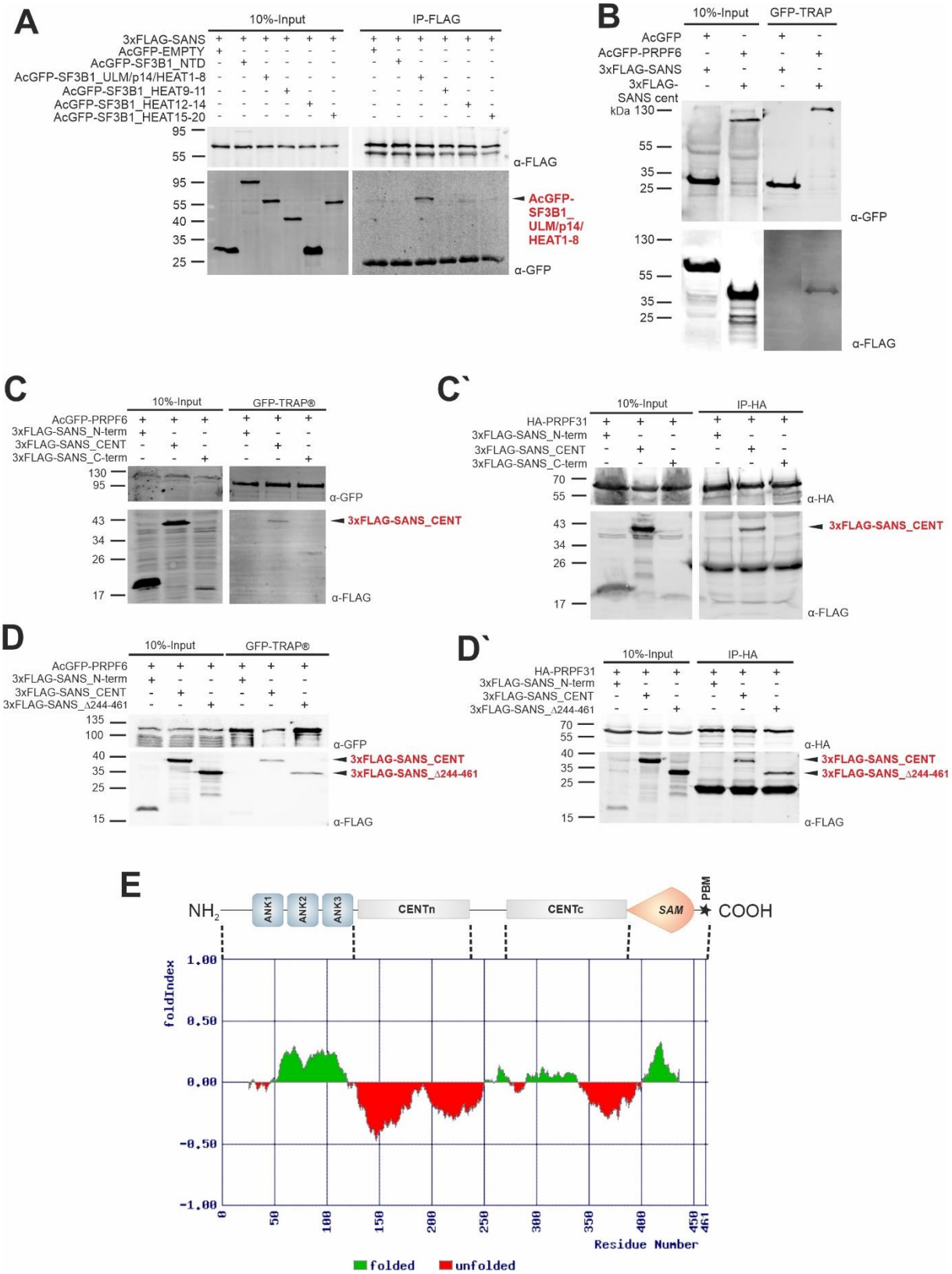

Figure S1. Analysis of SANS domains interacting with splicing factors SF3B1, PRPF6 and PRPF31. A) Western blot analysis of anti-FLAG immunoprecipitation from HEK293T cells expressing 3xFLAG-SANS and different truncation variants of SF3B1. SANS interacts with the SF3B1 central region including parts of the ULM, p14-binding and HEAT1-8 domains. **B)** Western blot analyses of GFP-TRAP® pull downs from cells co-expressing AcGFP-PRPF6 or AcGFP and SANS full length, respectively. Data indicates that only SANS full length interacts with AcGFP-PRPF6 but not with the AcGFP tag or beads of the GFP-TRAP®s. **C-C`)** Western blot analyses of GFP-TRAP® or anti-HA pull downs from cells co-expressing AcGFP-PRPF6 or HA-PRPF31 and SANS truncation variants, respectively. Data indicates that only SANS CENT domain, but not its N-terminal or C-terminal domains, interacts with PRPF6 **(C)** and PRPF31 **(C`). D-D`)** Western blot analyses of GFP-TRAP® and anti-HA pull downs from cells co-expressing AcGFP-PRPF6 or HA-PRPF31 together with SANS_Δ244-461 lacking the CENTc and downstream domains. Pull downs show that the SANS CENTn domain is essential for the interactions between SANS and PRPF6 **(D)** and PRPF31 **(D`)**. **E)** Graphical representation of the folding probability for SANS domains computed with the FoldIndex© online prediction tool. CENTn domain is a putative intrinsically disordered region. **A, C-D`**: numbers molecular weights in kDa.

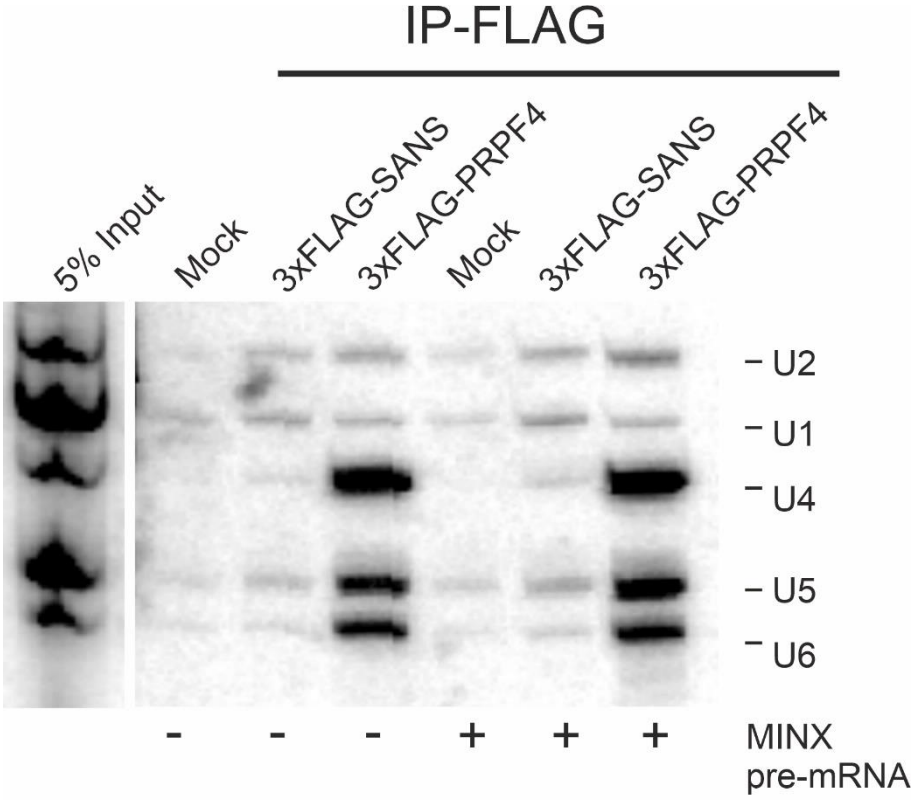

Figure S2. Analysis of the interaction of SANS with spliceosomal snRNAs. Northern blot analysis of isolated RNA from anti-FLAG immunoprecipitations from nuclear extracts of HEK293T cells expressing 3xFLAG-tagged SANS or PRPF4 in the absence in the presence of MINX pre-mRNA (under *in vitro* splicing conditions) using snRNA probes (U1, U2, U4, U5, and U6). In contrast to PRPF4, SANS does not strongly bind to U4/U6.U5 tri-snRNPs in normal conditions but shows lightly increased binding to snRNAs under *in vitro* splicing conditions after adding MINX pre-mRNA.

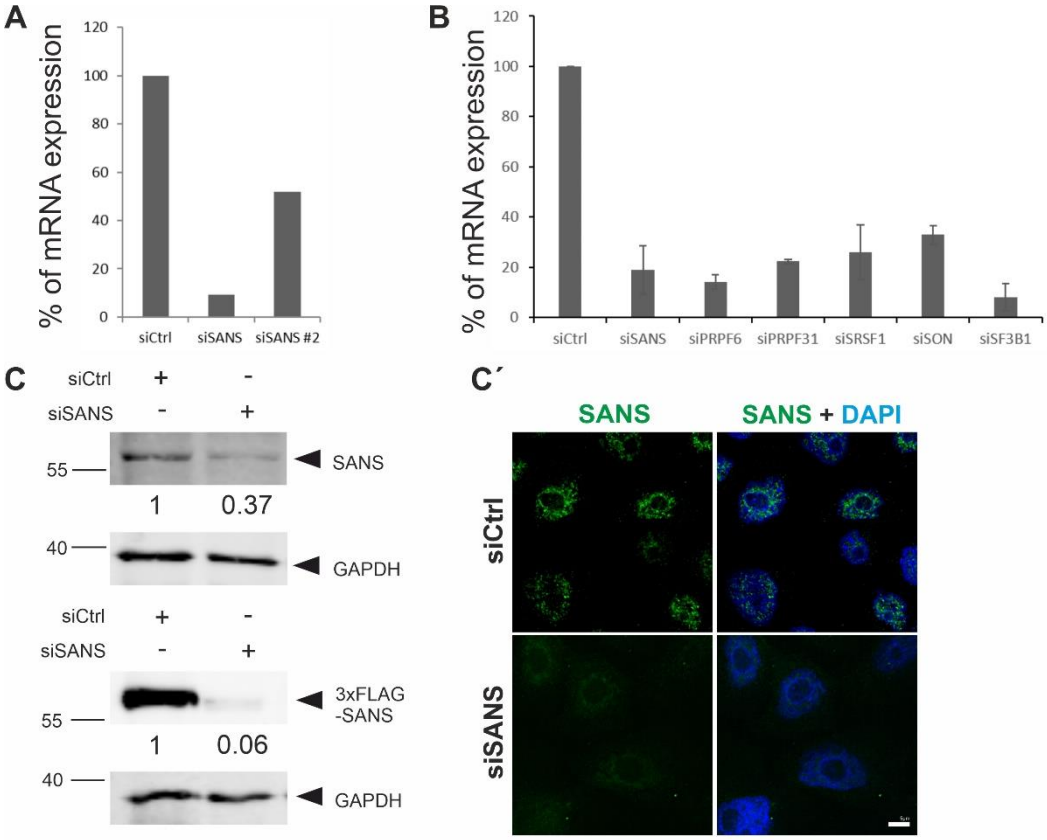
A
% of mRNA expression
120
100
80
60
40
20
0
siCtrl
siSANS
siSANS #2
B
% of mRNA expression
siCtrl
siSANS
siPRPF6
siPRPF31
siSRSF1
siSON
siSF3B1
C
siCtrl + -
siSANS - +
55
SANS
1 0.37
40
GAPDH
siCtrl + -
siSANS - +
55
3xFLAG -SANS
1 0.06
40
GAPDH
C´
SANS
SANS + DAPI
siCtrl
siSANS

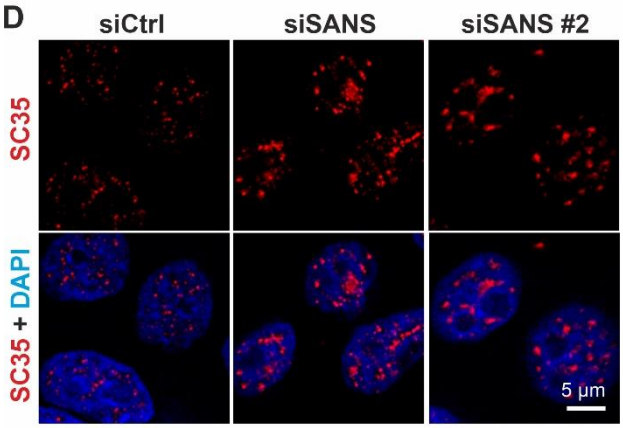
D
siCtrl
siSANS
siSANS #2
SC35
SC35 + DAPI
5 µm

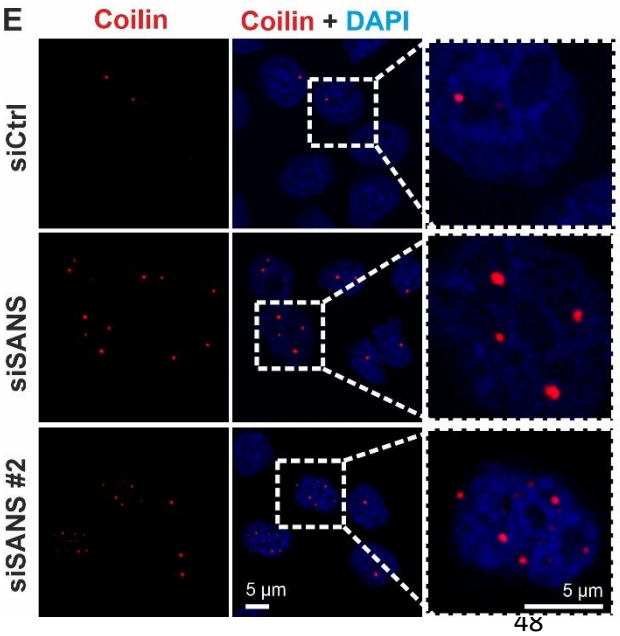
E
Coilin
Coilin + DAPI
siCtrl
siSANS
siSANS #2
5 µm
5 µm

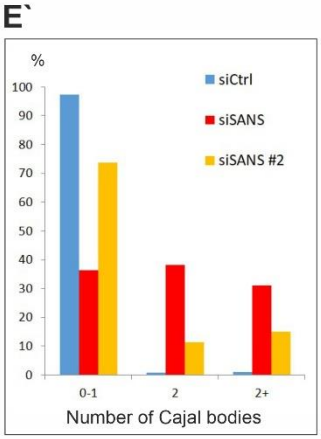
E`
%
100
90
80
70
60
50
40
30
20
10
0
siCtrl
siSANS
siSANS #2
0-1
2
2+
Number of Cajal bodies

Figure S3. Analysis of SANS knockdown on mRNA and protein levels in HEK293T cells. A) Quantitative PCR (qPCR) analysis of SANS mRNA expression in HEK293T cells treated with two different siRNAs (siSANS, siSANS #2). While siSANS leads to ~90% depletion, siSANS #2 only decreased the level of SANS mRNA to 50%. Thus, we used siSANS for further experiments. **B)** Representative qPCR analysis of mRNA expressions from three independent experiments. The siRNA-mediated knockdowns of SANS, PRPF6, PRPF31, SRSF1, SON, and SF3B1 resulted in ~80% decrease in mRNA levels. **C)** Western blot analysis of SANS-depleted HEK293T cells. siRNA knockdown of SANS leads to 60% decrease in the protein level of intrinsic SANS (RpAb). In addition, FLAG-SANS cannot be overexpressed in siSANS-treated cells indicating the specificity of the siRNA. **C`)** Immunofluorescence analysis of SANS-depleted HeLa cells. SANS (RpAb) signal disappeared from siSANS-depleted cells. **D)** Immunofluorescence staining of nuclear speckles of SC35 in the cells depleted of SANS applying siSANS or siSANS #2 siRNAs, respectevely. Both of siRNA depletions show enlarged nuclear speckle signals. Blue, DAPI counterstaining of nuclear DNA. **E)** Immunofluorescence staining for Cajal bodies (Coilin, red) in SANS-depleted HEK293T cells using siSANS or siSANS #2 siRNAs. **E`)** Quantification of the number of Cajal bodies in SANS-depleted cells; the graph shows the percentage of cells containing 0-1, 2 or more Cajal bodies. siSANS increased the number of Cajal bodies more efficiently than siSANS #2.

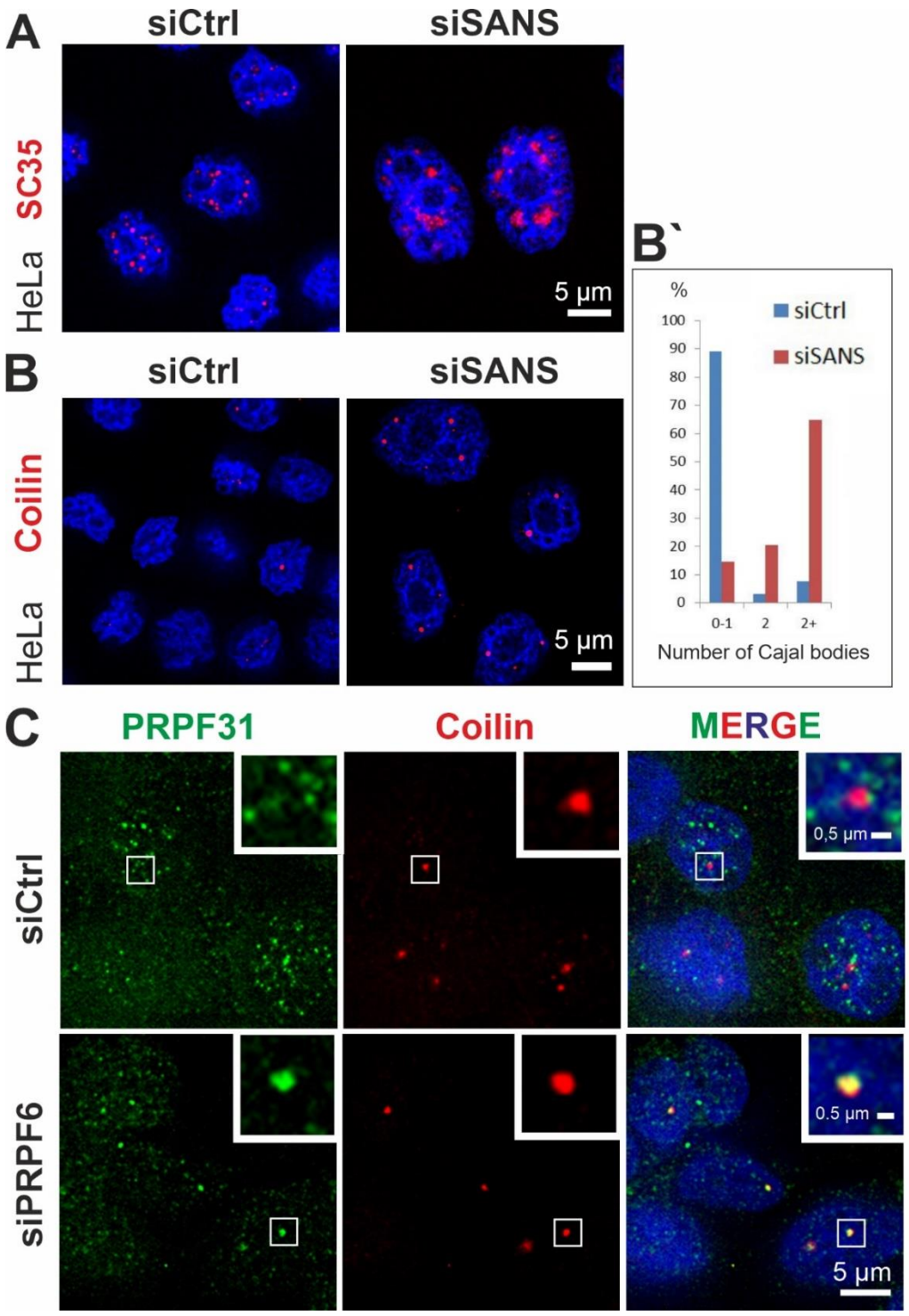

Figure S4. The effect of SANS and PRPF6 depletion on nuclear bodies in HEK293T and HeLa cells. A) Immunofluorescence of SC35 (red) in siRNA-treated HeLa cells counterstained with DAPI (blue). Nuclear speckles size increases in cells depleted of SANS (siSANS) compared with control siRNA-treated cells (siCtrl). **B)** Immunofluorescence staining for Cajal bodies (Coilin, red) in SANS-depleted HeLa cells. **B`)** Quantification of the number of Cajal bodies in SANS-depleted cells; the graph shows the percentage of cells containing 0-1, 2 or more Cajal bodies. SANS depletion increases the number of Cajal bodies in the nucleus. **C)** Double immunofluorescence staining of PRPF31 and Coilin in siCtrl- or siPRPF6-treated cells.

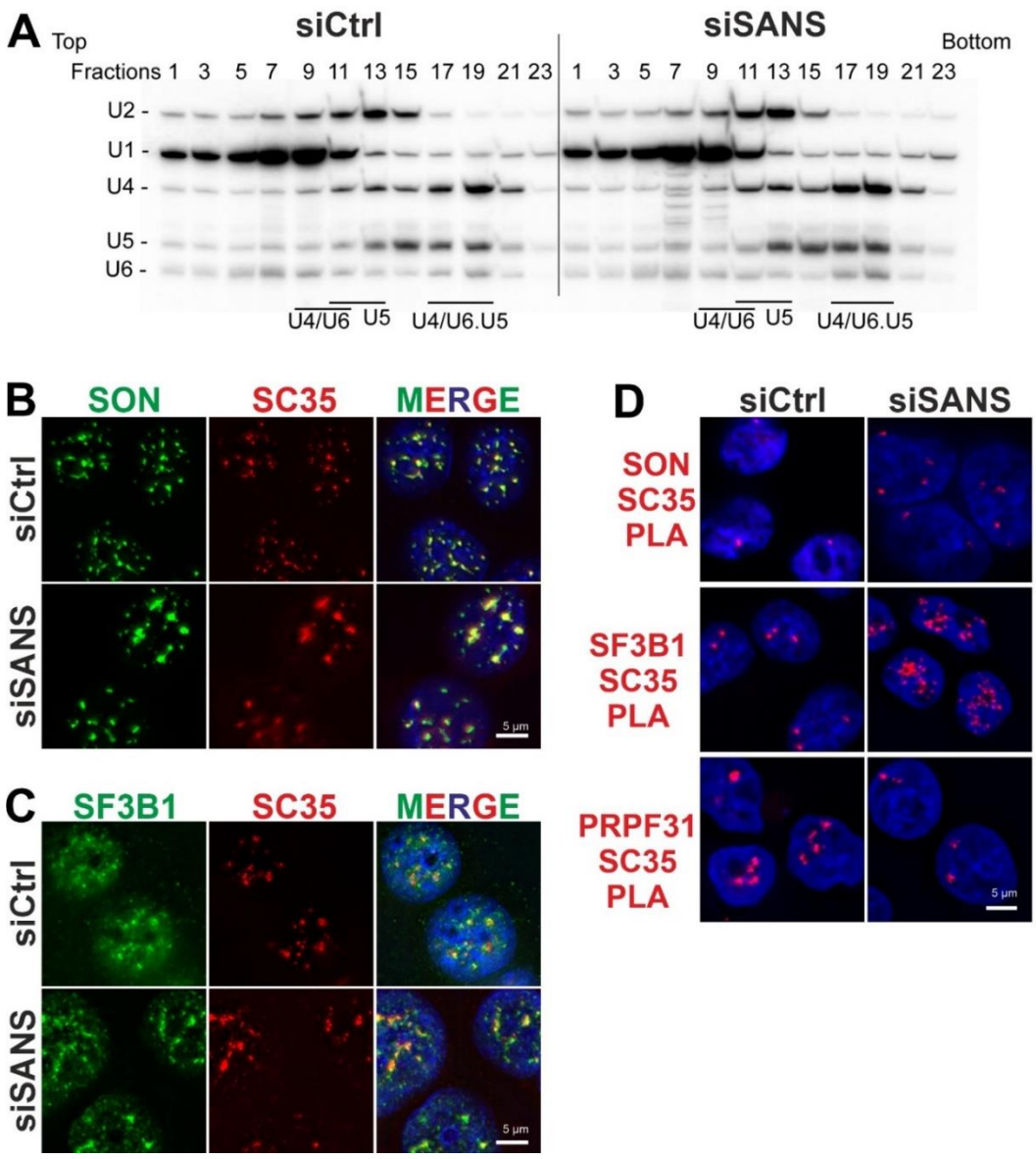

Figure S5. SANS depletion affects the nuclear speckle composition. A) Northern blot analysis of snRNAs isolated from a glycerol gradient (10-30%) fractionations of nuclear extracts from siCtrl- and siSANS-treated cells by applying oligonucleotide probes against U1, U2, U4, U5 and U6 snRNAs. The comparison of the distribution patterns of snRNPs across the gradients shows no accumulation of U4/U6 or U5 snRNPs indicating no significant deficit in the formation of the U4/U6.U5 tri-snRNP complex in SANS-depleted nuclear extract (Lane 17-19). However, a slight increase in the amount of tri-snRNPs is detected in the SANS-depleted extract (fraction 17). **B-C)** Immunofluorescence analysis shows increased staining of SON and SF3B1 in nuclear speckles (stained by anti-SC35) in SANS-depleted cells, when compared with siCtrl-treated cells. **D)** PLAs of SON-, SF3B1- and PRPF31-SC35 reveal increase of PLA signals for SON- and SF3B1-SC35 PLA pairs, but a decrease for PRPF31-SC35 confirming accumulations of SON and SF3B1 and the lack of PRPF31 in nuclear speckles of SANS-depleted cells.

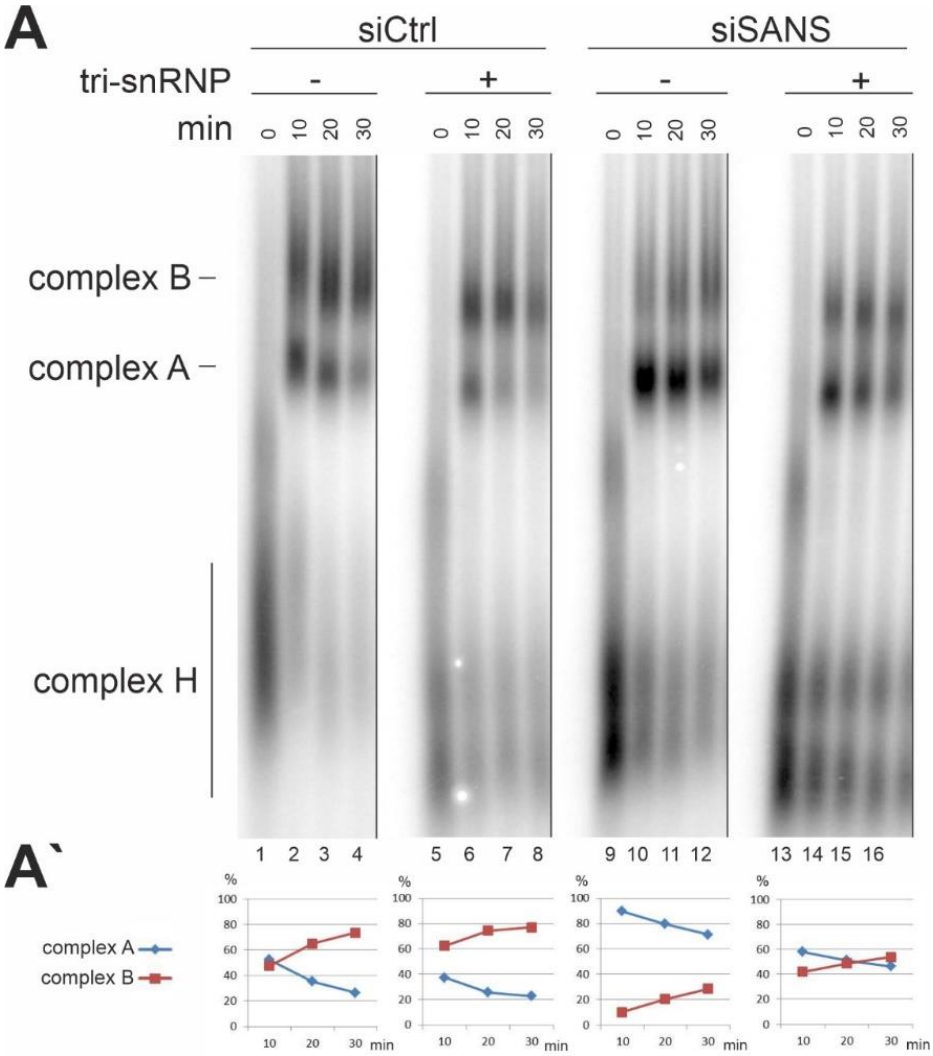

Figure S6. The purified tri-snRNP complex chases the stalled complex A to complex B in SANS-depleted nuclear extracts. A) Autoradiography of spliceosomal complexes assembled on ^{32}P-radiolabelled MINX pre-mRNA in control and SANS-depleted nuclear extracts analyzed by native agarose gel electrophoresis. Splicing reactions were incubated at 30 °C for the indicated time points (0-30 min) and stopped by the addition of heparin. Where indicated the purified tri-snRNP complex is added to the reaction before addition of MINX pre-mRNA at 0 min time point. Positions of spliceosomal complexes H, A, and B are indicated. **A`)** Quantification of the percentage of spliceosomal complexes A and B at each time point. In SANS-depleted nuclear extracts addition of purified tri-snRNPs chased the accumulated complex A to complex B (Lane 9-16).

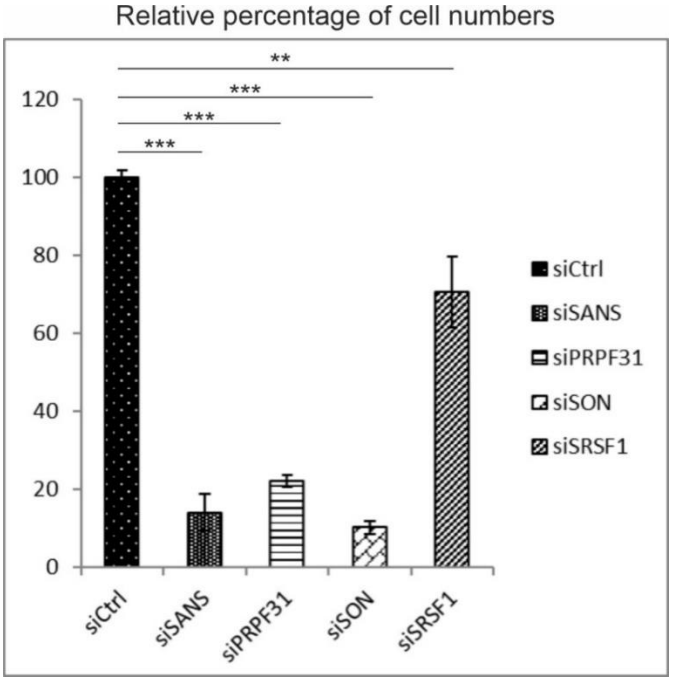

Figure S7. SANS depletion affects cell proliferation. WST1 cell proliferation assay for cells depleted of SANS, SON, PRPF31 or SRSF1 by siRNA-mediated knockdown. siSANS, siSON and siPRPF31 reduce the proliferation rate by 80% when compared with control (siCtrl). In contrast, siSRSF1 reduces the proliferation rate only by less than 20%. (**: $p<0.005$, ***: $p<0.001$)